

2010

# The Jets of TeV Blazars at Higher Resolution: 43 GHz and Polarimetric VLBA Observations from 2005-2009

B. Glenn Piner
gpiner@whittier.edu

Philip G. Edwards

The Astrophysical Journal, 797:25 (16pp), 2014 December 10 doi:10.1088/0004-637X/797/1/25


# FIRST-EPOCH VLBA IMAGING OF 20 NEW TeV BLAZARS

B. Glenn Piner[1,2] and Philip G. Edwards[3]
[1] Department of Physics and Astronomy, Whittier College, 13406 E. Philadelphia Street, Whittier, CA 90608, USA; gpiner@whittier.edu
[2] Jet Propulsion Laboratory, California Institute of Technology, 4800 Oak Grove Drive, Pasadena, CA 91106, USA
[3] CSIRO Astronomy and Space Science, Australia Telescope National Facility, P.O. Box 76, Epping, NSW 1710, Australia
*Received 2014 August 18; accepted 2014 September 30; published 2014 November 21*

## ABSTRACT

We present Very Long Baseline Array (VLBA) images of 20 TeV blazars not previously well studied on the parsec scale. All 20 of these sources are high-frequency peaked BL Lac objects (HBLs). Observations were made between August and December of 2013 at a frequency of 8.4 GHz. These observations represent the first epoch of a VLBA monitoring campaign on these blazars, and they significantly increase the fraction of TeV HBLs studied with high-resolution imaging. The peak very long baseline interferometry (VLBI) flux densities of these sources range from $\sim$10 to $\sim$100 mJy bm$^{-1}$, and parsec-scale jet structure is detected in all sources. About half of the VLBI cores are resolved, with brightness temperature upper limits of a few times $10^{10}$ K, and we find that a brightness temperature of $\sim 2 \times 10^{10}$ K is consistent with the VLBI data for all but one of the sources. Such brightness temperatures do not require any relativistic beaming to reduce the observed value below commonly invoked intrinsic limits; however, the lack of detection of counterjets does place a modest limit on the bulk Lorentz factor of $\gamma \gtrsim 2$. These data are thus consistent with a picture where weak-jet sources like the TeV HBLs develop significant velocity structures on parsec scales. We also extend consideration to the full sample of TeV HBLs by combining the new VLBI data with VLBI and gamma-ray data from the literature. By comparing measured VLBI and TeV fluxes to samples with intrinsically uncorrelated luminosities generated by Monte Carlo simulations, we find a marginally significant correlation between the VLBI and TeV fluxes for the full TeV HBL sample.

*Key words:* BL Lacertae objects: general – galaxies: active – galaxies: jets – radio continuum: galaxies

*Online-only material:* color figures

## 1. INTRODUCTION

The number of TeV blazars has grown rapidly in recent years (see, e.g., the reviews of Holder 2012, 2014) with 54 TeV blazars currently known.[4] The vast majority of these (44 of 54, or about 80%) belong to the blazar subclass of high-frequency peaked BL Lac objects, or HBLs. Several of these TeV HBLs have displayed remarkable variability in their TeV gamma-ray emission on timescales as short as a few minutes (e.g., Aharonian et al. 2007c; Albert et al. 2007c; Sakamoto et al. 2008). Although various explanations have been proposed for such rapid variability (e.g., Begelman et al. 2008; Nalewajko et al. 2011; Narayan & Piran 2012; Barkov et al. 2012), they share the common feature of high bulk Lorentz factors of at least $\gtrsim$25 for the gamma-ray emitting plasma in their relativistic jets. High bulk Lorentz factors and Doppler factors are also required to model TeV blazar spectral energy distributions (SEDs; e.g., Tavecchio et al. 2010), particularly in the case of one-zone models. For example, fitting the SED of the TeV blazar PKS 1424+240 with a one-zone model yields a Doppler factor of $\delta \sim 100$ (Aleksić et al. 2014a).

Direct imaging of the jets of these blazars on parsec scales requires very long baseline interferometry (VLBI). Most HBLs are relatively faint in the radio, so the TeV HBLs are not well represented in large VLBI monitoring projects, such as MOJAVE (Lister et al. 2009). We have previously reported multiepoch VLBI kinematic results for 11 established TeV HBLs (Piner et al. 2010; Tiet et al. 2012). A major result of those kinematic analyses was the absence of any rapidly moving features in the jets of those blazars; all components in all 11 sources were either stationary or slowly moving ($\lesssim 1c$). Slow apparent speeds of VLBI components in specific TeV HBLs have been confirmed by numerous other studies (e.g., Giroletti et al. 2004a; Lico et al. 2012; Blasi et al. 2013; Aleksić et al. 2013; Richards et al. 2013), although note that TeV-detected intermediate-peaked BL Lac objects (IBLs), such as 3C 66A and BL Lac, do show apparently superluminal components (e.g., Britzen et al. 2008). While effects other than slow bulk motion can produce slow apparent speeds of components, the complete absence of any rapidly moving features in all of these jets, after as much as 20 yr of Very Long Baseline Array (VLBA) monitoring (for Mrk 421 and Mrk 501), and even after powerful flares (Richards et al. 2013), is quite distinct from the behavior of other types of gamma-ray blazars, which show frequent superluminal ejections (e.g., Lister et al. 2009; Marscher 2013). Taken with other measured radio properties, such as the brightness temperatures and core dominance (Giroletti et al. 2004b; Lister et al. 2011), the VLBI data imply only modest bulk Lorentz factors and Doppler factors in the parsec-scale radio jets of these TeV HBLs. (Note that because the sources appear one-sided on parsec scales, the VLBI data do require that the sources be at least moderately relativistic.) This discrepancy between the Doppler and Lorentz factors estimated from the gamma-ray data and the radio data has been referred to as the "Doppler Crisis" of TeV blazars.

A natural explanation for the Doppler Crisis is that the radio and gamma-ray emission may be produced in different parts of the jet with different bulk Lorentz factors. Several variations of such a multicomponent jet have been proposed, including decelerating jets (Georganopoulos & Kazanas 2003), spine-sheath structures (Ghisellini et al. 2005), minijets within the main jet (Giannios et al. 2009), and faster moving leading edges

[4] http://tevcat.uchicago.edu/

of blobs (Lyutikov & Lister 2010), but they all require that the jets of HBLs contain significant velocity structures. Some of these velocity structures, such as a fast spine and slower layer, may under certain conditions produce observable signatures in VLBI images, such as limb brightening of the transverse jet structure. Limb brightening has indeed been observed in VLBI images of the bright TeV blazars Mrk 421 and Mrk 501 (e.g., Giroletti et al. 2004a, 2006, 2008; Piner et al. 2009, 2010; Croke et al. 2010; Blasi et al. 2013).

These arguments for velocity structures in the jets of TeV HBLs are independently supported by developments in radio-loud active galactic nucleus (AGN) unification (Meyer et al. 2011, 2013a; see also Ghisellini et al. 2009). In that unification work, radio-loud AGNs are divided into two distinct subpopulations that constitute a broken power sequence. The weak jet subpopulation resulting from inefficient accretion modes (and corresponding to HBLs when viewed at a small angle) follows a debeaming curve that requires velocity gradients in the jets, such as a decelerating or spine-sheath jet; see also the similar arguments in earlier unification work (Chiaberge et al. 2000). The TeV HBLs may thus represent the small viewing angle peak of a distinct radio-loud population with both fundamentally different jet structure and accretion mode from the more powerful blazars. If this is the case, then obtaining more information on the parsec-scale structure of these sources through high-resolution imaging is quite important.

We are presently taking advantage of both the rapidly growing TeV blazar source list and the recently upgraded sensitivity of the VLBA to significantly expand our previous work on the parsec-scale structure of TeV HBLs (e.g., Piner et al. 2010; Tiet et al. 2012). Here, we present first-epoch VLBA images of 20 newer TeV HBLs discovered during the years 2006 to 2013, several of which had never been imaged with VLBI. This represents the first stage of a multiepoch VLBA monitoring program on these sources designed to provide parsec-scale kinematic and structural information on nearly the complete sample of TeV HBLs. In Section 2, we describe the source selection and observations; in Section 3, we present the results for these observations; and in Section 4, we extend consideration to the full set of TeV HBLs. Final discussion and conclusions are given in Section 5.

## 2. OBSERVATIONS

### 2.1. Source Selection

We have been conducting VLBA observations of TeV-detected HBLs since the discovery of the first two TeV blazars (Mrk 421 and Mrk 501) in the 1990s in order to study their jet physics through high-resolution parsec-scale imaging (see Section 1). Our complete candidate source list is thus the 44 HBLs listed as detections in the TeVCat catalog[5] as of this writing. From those 44 sources we excluded the following for the observations in this paper.

1. Eleven sources reported as TeV detections before 2007 for which we have already published multiepoch VLBA observations: six of these sources are discussed by Piner et al. (2010), and an additional five by Tiet et al. (2012).
2. Seven sources that have sufficient multiepoch VLBA data in the MOJAVE monitoring program.[6]
3. Three sources that are below $-40^\circ$ declination and thus difficult to image with the VLBA.
4. Two sources that were detected too recently (after 2013) to be included in this work.
5. The low brightness temperature source HESS J1943+213 (Gabányi et al. 2013).

These exclusions are shown in tabular form in Table 1, and they leave 20 HBLs (or nearly half of the full sample) that were all reported as new detections by the TeV telescopes between 2006 and 2013 and that have not yet been studied with multiepoch VLBI imaging by any program. The goal of the observations presented here is to provide high-dynamic-range single-epoch images of these 20 sources, as a precursor to a multiepoch monitoring program to study the jet kinematics.

Single-epoch pilot images of 8 of these 20 sources, obtained prior to the VLBA sensitivity upgrade (Romney et al. 2009), were presented by Piner & Edwards (2013). For those eight sources, we present in this paper the first epoch of a multiepoch monitoring series obtained after the sensitivity upgrade and with images of significantly higher dynamic range than those in Piner & Edwards (2013). For the remaining 12 sources, we present the pilot images made to assess suitability for multiepoch monitoring, all of which were made subsequent to the VLBA sensitivity upgrade.

The VLBI and gamma-ray properties of the entire sample of 44 TeV HBLs are discussed later in this paper (see Section 4 and Table 7).

### 2.2. Details of Observations

Details of the observing sessions are given in Table 2. All observations were made at an observing frequency of 8.4 GHz (4 cm) because this provides the optimum combination of angular resolution and sensitivity for these fainter sources. All observations used the full 2 Gbps recording rate of the VLBA and were made using the polyphase filterbank observing system of the Roach Digital Backend in its dual-polarization configuration of eight contiguous 32 MHz channels at matching frequencies in each polarization. Although dual polarization was recorded, only total intensity (Stokes *I*) was calibrated and imaged because of the likely submillijansky level of polarized flux from most of these sources.

We used phase referencing for three of the fainter targets: SHBL J001355.9−185406, 1ES 0347−121, and 1RXS J101015.9−311909; we did this because their correlated flux densities were uncertain and to obtain precise milliarcsecond-scale positions because they were not in the VLBA input catalog. These data were phase referenced to the International Celestial Reference Frame (ICRF) sources J0015−1812, J0351−1153, and J1011−2847, respectively, all of which had separations of less than $3^\circ$ from the target sources. Based on the ICRF positions of the calibrator sources, we derived (J2000) positions of R.A. $= 00^{\rm h}13^{\rm m}56\overset{\rm s}{.}043$, decl. $= -18^\circ54'06\overset{''}{.}696$ for SHBL J001355.9−185406, R.A. $= 03^{\rm h}49^{\rm m}23\overset{\rm s}{.}186$, decl. $= -11^\circ59'27\overset{''}{.}361$ for 1ES 0347−121, and R.A. $= 10^{\rm h}10^{\rm m}15\overset{\rm s}{.}979$, decl. $= -31^\circ19'08\overset{''}{.}408$ for 1RXS J101015.9−311909, which we expect to be accurate to a few milliarcseconds. Although those observations were done in phase-referencing mode, all three sources were bright enough for fringe fitting, and the fringe-fit data were used in the subsequent imaging.

We used the AIPS software package for calibration and fringe fitting of the correlated visibilities, and fringes were found across the full bandwidth at significant signal-to-noise ratios and

[5] http://tevcat.uchicago.edu/
[6] http://www.physics.purdue.edu/astro/MOJAVE/allsources.html

**Table 1**
Sample Selection

| Source[a] | Included[b] | Reason[c] | Source[a] | Included[b] | Reason[c] |
|---|---|---|---|---|---|
| SHBL J001355.9−185406 | Y | ... | Markarian 421 | N | 1 |
| KUV 00311−1938 | Y | ... | Markarian 180 | N | 1 |
| 1ES 0033+595 | Y | ... | RX J1136.5+6737 | N | 4 |
| RGB J0136+391 | Y | ... | 1ES 1215+303 | N | 2 |
| RGB J0152+017 | Y | ... | 1ES 1218+304 | N | 1 |
| 1ES 0229+200 | Y | ... | MS 1221.8+2452 | Y | ... |
| PKS 0301−243 | N | 2 | 1ES 1312−423 | N | 3 |
| IC 310 | N | 2 | PKS 1424+240 | N | 2 |
| RBS 0413 | Y | ... | H 1426+428 | N | 1 |
| 1ES 0347−121 | Y | ... | 1ES 1440+122 | Y | ... |
| 1ES 0414+009 | Y | ... | PG 1553+113 | N | 1 |
| PKS 0447−439 | N | 3 | Markarian 501 | N | 1 |
| 1ES 0502+675 | Y | ... | H 1722+119 | Y | ... |
| PKS 0548−322 | Y | ... | 1ES 1727+502 | N | 2 |
| RX J0648.7+1516 | Y | ... | 1ES 1741+196 | Y | ... |
| 1ES 0647+250 | Y | ... | HESS J1943+213 | N | 5 |
| RGB J0710+591 | Y | ... | 1ES 1959+650 | N | 1 |
| 1ES 0806+524 | N | 2 | PKS 2005−489 | N | 3 |
| RBS 0723 | N | 4 | PKS 2155−304 | N | 1 |
| 1RXS J101015.9−311909 | Y | ... | B3 2247+381 | Y | ... |
| 1ES 1011+496 | N | 2 | 1ES 2344+514 | N | 1 |
| 1ES 1101−232 | N | 1 | H 2356−309 | N | 1 |

**Notes.**
[a] Source names are the so-called canonical name used by TeVCat.
[b] Whether or not the source is included in the new observations for this paper.
[c] Reason for exclusion: 1: monitored in our previous work, 2: in MOJAVE program, 3: too far south, 4: detection too recent, 5: low brightness temperature (see Section 4.2).

**Table 2**
Observation Log

| Date | Observation Code | Observing Time (hr) | Excluded VLBA Antennas[a] | Target Sources |
|---|---|---|---|---|
| 2013 Aug 16 | S6117D1 | 6 | FD,LA | SHBL J001355.9−185406, 1ES 0033+595 |
| 2013 Aug 23 | S6117A1 | 8 | None | RGB J0152+017, 1ES 0229+200, RBS 0413, 1ES 0347−121 |
| 2013 Aug 30 | S6117D2 | 6 | None | KUV 00311−1938, RGB J0136+391 |
| 2013 Sep 19 | S6117B1 | 8 | KP | 1ES 0414+009, 1ES 0502+675, PKS 0548−322, RGB J0710+591 |
| 2013 Oct 21 | S6117D3 | 6 | LA | RX J0648.7+1516, 1ES 0647+250 |
| 2013 Oct 24 | S6117D4 | 6 | FD,LA | 1RXS J101015.9−311909, MS 1221.8+2452 |
| 2013 Dec 23 | S6117D5 | 9 | KP,NL | 1ES 1440+122, H 1722+119, 1ES 1741+196, B3 2247+381 |

**Notes.**
[a] VLBA antennas that did not participate or that were excluded from the imaging for that session. FD = Fort Davis, Texas; KP = Kitt Peak, Arizona; LA = Los Alamos, New Mexico; NL = North Liberty, Iowa.

small delays and rates to all target sources. A small number of discrepant visibilities were flagged, and the final images were produced using CLEAN and self calibration in the DIFMAP software package. VLBA imaging of sources at these lower flux density levels can be sensitive to the self-calibration averaging interval, and self calibration will generate spurious point-source structure if the averaging interval is too short (e.g., Martí-Vidal & Marcaide 2008). We carefully investigated and selected self-calibration solution intervals for the fainter sources to make sure that minimal spurious flux density (less than ∼1 mJy) should be introduced into the images through self calibration (see Equations (7) and (8) of Martí-Vidal & Marcaide 2008). In the section below, all images are displayed using natural weighting in order to maximize the dynamic range. At a typical redshift for these sources of $z \sim 0.2$, 1 milliarcsecond (a typical beam size) corresponds to a linear resolution of about 3 pc, and the smallest sizes measurable in model fitting (about 10% of the beam size) would have a linear size of about 0.3 pc.

## 3. RESULTS FOR THE 20 NEW SOURCES

### *3.1. Images*

The VLBA images of the 20 TeV HBLs studied for this paper are shown in Figure 1, and the parameters of these images are tabulated in Table 3. The B1950 name is shown in each panel in Figure 1 and may be used subsequently to refer to the source. All sources show a bright, compact component, hereafter identified

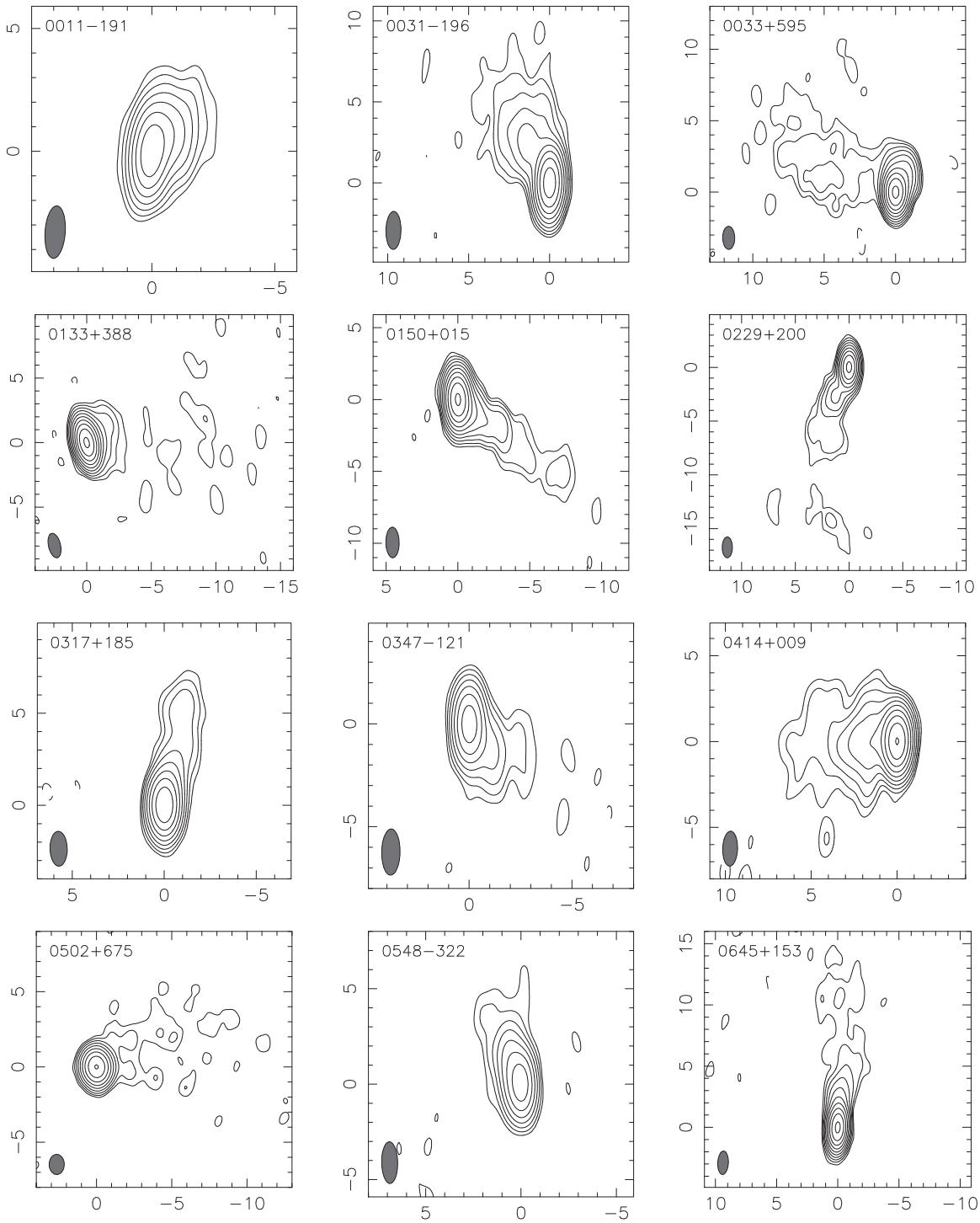


**Figure 1.** VLBA images at 8.4 GHz of TeV blazars from Table 3. Parameters of the images are given in Table 3. Axes are in milliarcseconds. The lowest contour in each images is three times the rms noise level from Table 3, and each subsequent contour is a factor of two higher.

as the VLBI core, and they all show additional extended structure that can be modeled by at least one Gaussian feature in addition to the core (see Section 3.2). Thus, all of these sources are suitable for continued VLBI monitoring to study the parsec-scale jet kinematics. The images in Figure 1 do not show the entire CLEANed region for clarity, but instead are zoomed in on the core and the inner jet region. Larger-scale images plus all associated data files are available at the project Web site.[7] The peak flux densities in the images in Figure 1 range from 7 to 98 mJy bm$^{-1}$ (see Table 3). However, the noise levels are quite low, typically only about 0.02 mJy bm$^{-1}$ (Table 3), close to the expected thermal noise limit for these observations, so even the images of the fainter sources have dynamic ranges of several hundred, which is easily high enough to image the parsec-scale jet structure.

About half of these sources have been previously imaged with the VLBA by other investigators, although all of those images were obtained prior to the VLBA sensitivity upgrade.

[7] www.whittier.edu/facultypages/gpiner/research/archive/archive.html

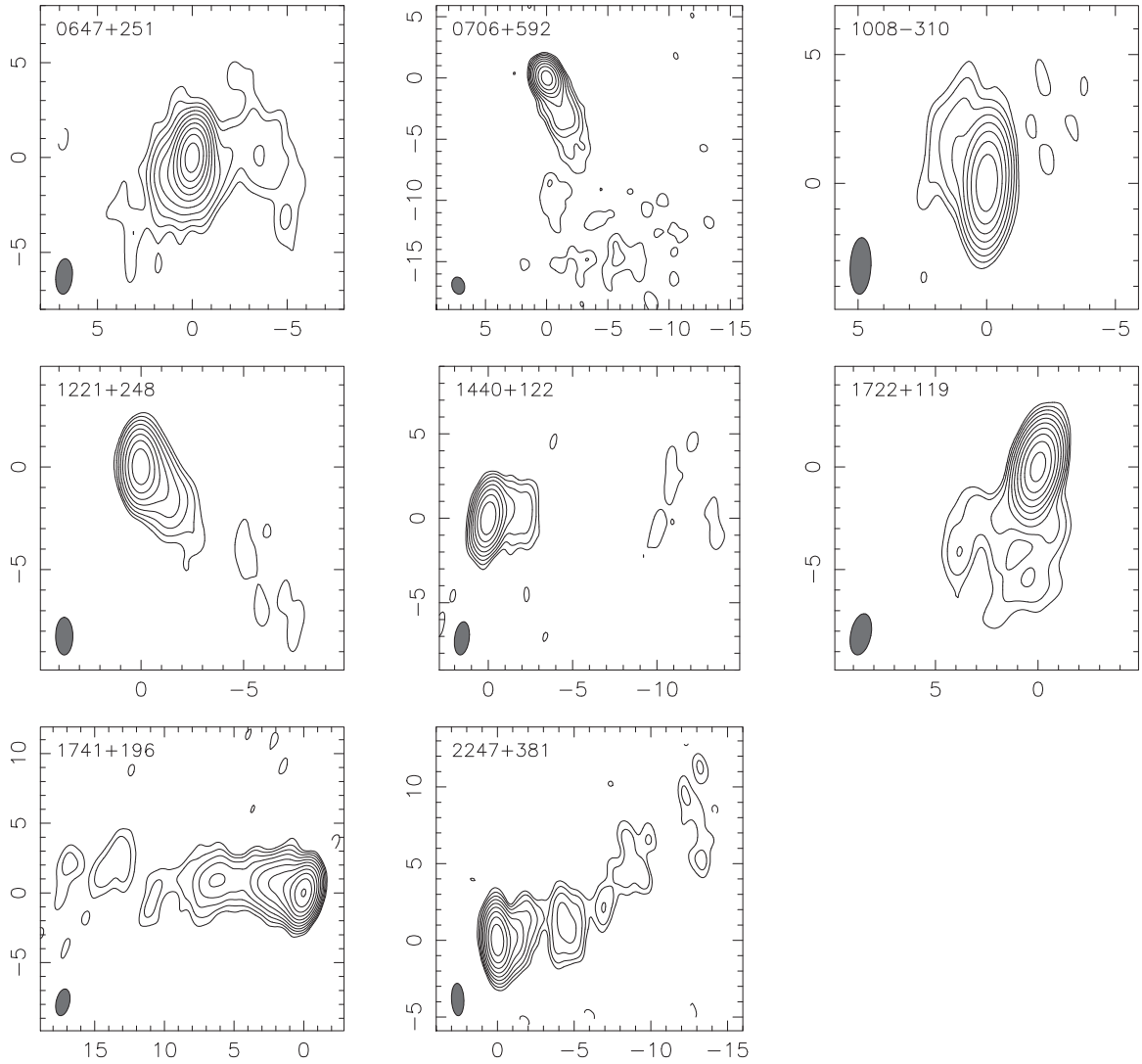


**Figure 1.** (Continued)

Rector et al. (2003) show 5 GHz VLBA images of the five sources 0033+595, 0229+200, 0414+009, 0647+251, and 1741+196. Those images have about twice the beam size and about three times the noise level of the images in Figure 1, but they all agree in showing the same general extended jet structure. Giroletti et al. (2004b) show 5 GHz VLBA images of the five sources 0229+200, 0347−121, 0548−322, 0706+592, and 1440+122; however, those images all have about six times the noise level of the images in Figure 1, and they only detect parsec-scale jet structure in 0706+592. The source 1722+119 has a single image in the MOJAVE database, but it shows only the VLBI core. Collectively, these prior imaging results for those 10 sources demonstrate the importance of the VLBA sensitivity upgrade in imaging the parsec-scale structure of the TeV HBLs. For the remaining 10 sources in Figure 1, these are the first published VLBI images known to the authors.

The general parsec-scale morphology of the sources in Figure 1 is familiar from VLBI studies of brighter TeV blazars, for example, Mrk 421 and Mrk 501 (Piner et al. 1999; Edwards & Piner 2002; Giroletti et al. 2006, 2008). Most of the sources show a collimated jet a few milliarcseconds long that transitions to a lower surface brightness, more diffuse jet with a broader opening angle at a few milliarcseconds from the core. The structure at tens of milliarcseconds from the core at 8 GHz then appears patchy and filamentary. As an example, the source 0706+592 nicely displays this morphology in Figure 1. Despite this general pattern, there are a couple of sources with unusual morphologies. The sources 0033+595 and 0647+251 both show structure on opposite sides of the presumed core. Either the brightest most compact component is not the core, the jet crosses back over the line of sight (as seen in the TeV blazar 1ES 1959+650 by Piner et al. 2008), or the emission is truly two-sided. Forthcoming imaging at multiple frequencies should identify the core for these unusual cases. At least two sources (0502+675 and 1722+119) also display limb-brightened jets in their inner jet region, which is discussed further in Section 3.5.

### *3.2. Model Fits*

After imaging and final calibration of the visibilities, we fit circular Gaussian models to the calibrated visibilities for each source using the *modelfit* task in DIFMAP. Circular Gaussians are more stable than elliptical Gaussians during fitting, and they provided adequate fits to the visibilities for all sources, as noted by the reduced chi-squared of the fit and visual inspection of the residual map and visibilities. Model fitting directly to the visibilities allows subbeam resolution to be obtained, and components can be clearly identified in the model fitting even

**Table 3**
Parameters of the Images

| Source | B1950 Name | Time On Source (minutes) | Beam Parameters[a] | Peak Flux Density (mJy bm$^{-1}$) | $I_{rms}$[b] (mJy bm$^{-1}$) |
|---|---|---|---|---|---|
| SHBL J001355.9−185406 | 0011−191 | 120 | 2.15,0.82,−4.1 | 10 | 0.029 |
| KUV 00311−1938 | 0031−196 | 144 | 2.34,0.93,−1.1 | 26 | 0.022 |
| 1ES 0033+595 | 0033+595 | 132 | 1.61,0.84,0.7 | 43 | 0.024 |
| RGB J0136+391 | 0133+388 | 150 | 1.93,0.93,13.3 | 35 | 0.020 |
| RGB J0152+017 | 0150+015 | 96 | 2.12,0.92,0.9 | 43 | 0.025 |
| 1ES 0229+200 | 0229+200 | 96 | 1.93,0.94,−0.2 | 21 | 0.023 |
| RBS 0413 | 0317+185 | 96 | 1.89,0.94,1.3 | 18 | 0.025 |
| 1ES 0347−121 | 0347−121 | 96 | 2.25,0.89,−0.9 | 7 | 0.025 |
| 1ES 0414+009 | 0414+009 | 104 | 2.04,0.87,−1.7 | 35 | 0.022 |
| 1ES 0502+675 | 0502+675 | 104 | 1.34,1.01,0.5 | 19 | 0.023 |
| PKS 0548−322 | 0548−322 | 104 | 2.19,0.84,1.0 | 20 | 0.062 |
| RX J0648.7+1516 | 0645+153 | 160 | 1.92,0.86,−3.0 | 36 | 0.020 |
| 1ES 0647+250 | 0647+251 | 160 | 1.88,0.88,−4.9 | 43 | 0.018 |
| RGB J0710+591 | 0706+592 | 104 | 1.42,1.03,14.5 | 28 | 0.023 |
| 1RXS J101015.9−311909 | 1008−310 | 120 | 2.20,0.81,−2.7 | 29 | 0.040 |
| MS 1221.8+2452 | 1221+248 | 132 | 1.83,0.84,−0.1 | 16 | 0.023 |
| 1ES 1440+122 | 1440+122 | 117 | 1.98,0.87,−7.2 | 18 | 0.025 |
| H 1722+119 | 1722+119 | 117 | 2.04,0.98,−11.8 | 66 | 0.030 |
| 1ES 1741+196 | 1741+196 | 117 | 1.95,0.97,−12.6 | 98 | 0.030 |
| B3 2247+381 | 2247+381 | 117 | 2.11,0.81,2.5 | 42 | 0.029 |

**Notes.**
[a] Numbers are for the naturally weighted beam and are the FWHMs of the major and minor axes in milliarcseconds and the position angle of the major axis in degrees. Position angle is measured from north through east.
[b] rms noise in the total intensity image.

when they appear blended with the core component or with each other in the CLEAN images. In a number of cases, patchy low surface brightness emission beyond the collimated jet region could not be well fit by a circular Gaussian, so the model fits do not necessarily represent the most distant emission seen on the CLEAN images. Note also that, because of incomplete sampling in the $(u, v)$ plane, VLBI model fits are not unique and represent only one mathematically possible deconvolution of the source structure.

The circular Gaussian models fit to all 20 sources are given in Table 4. Note that flux values for closely spaced components may be inaccurate because it is difficult for the fitting algorithm to uniquely distribute the flux during model fitting. The model component naming follows the scheme used in our previous papers (e.g., Piner et al. 2010); jet components are numbered C1, C2, and so on from the outermost component inward. Observer-frame brightness temperatures are also given in Table 4 for all partially resolved core components (those for which the best-fit size is not zero). These VLBI core brightness temperatures and associated errors are discussed in detail in the following subsection.

### 3.3. Core Brightness Temperatures

The observed brightness temperatures of VLBI cores can be used to constrain both Doppler beaming factors and the physical processes occurring in a source. The maximum observer-frame brightness temperature of a circular Gaussian is

$$T_B = 1.22 \times 10^{12} \frac{S}{a^2 \nu^2} \text{ K}, \quad (1)$$

where $S$ is the flux density of the Gaussian in janskys, $a$ is the FWHM of the Gaussian in milliarcseconds, and $\nu$ is the observing frequency in GHz. Note that we use observer-frame brightness temperatures, i.e., without applying the $(1 + z)$ factor to convert to source-frame brightness temperatures, because the redshift of a number of these sources is uncertain (see Table 7). The median redshift of the sources with known redshift is about 0.2, so source-frame brightness temperatures are only about 20% higher.

Several mechanisms can act to limit the intrinsic rest-frame brightness temperature of a synchrotron source, for example, rapid energy loss by inverse Compton emission that limits the brightness temperature to $\sim 5 \times 10^{11}$–$1 \times 10^{12}$ K (Kellermann & Pauliny-Toth 1969) or equipartition of energy between particles and magnetic fields that limits the brightness temperature to $\sim 5 \times 10^{10}$–$1 \times 10^{11}$ K (Readhead 1994). The observed brightness temperature of a source is increased relative to its intrinsic brightness temperature by a factor of the Doppler factor $\delta$.[8] Thus, if upper limits to the intrinsic brightness temperature are known, then the observed brightness temperature can be used to compute a lower limit to the Doppler factor. Similarly, if the Doppler factor can be estimated by independent means, then intrinsic brightness temperatures can be computed from observed values. This has been done by, e.g., Lähteenmäki et al. (1999), Homan et al. (2006), and Hovatta et al. (2013), who all used either apparent superluminal speeds or total flux density variability to compute intrinsic brightness temperatures of AGN samples. All of these studies concluded that typical intrinsic brightness temperatures were in the range of a few times $10^{10}$–$10^{11}$ K and therefore were likely to be limited by equipartition of energy.

[8] The Doppler factor $\delta = 1/(\gamma(1 - \beta \cos\theta))$, where $\theta$ is the viewing angle, $\beta = v/c$, and $\gamma = (1 - \beta^2)^{-1/2}$ is the bulk Lorentz factor.

**Table 4**
Circular Gaussian Models

| Source | B1950 Name | Component | $S$ | $r$ | P.A. | $a$ | $\chi^2_R$ | $T_B$ |
|---|---|---|---|---|---|---|---|---|
| | | | (mJy) | (mas) | (deg) | (mas) | | ($10^{10}$ K) |
| (1) | (2) | (3) | (4) | (5) | (6) | (7) | (8) | (9) |
| SHBL J001355.9−185406 | 0011−191 | Core | 9.3 | ... | ... | 0.23 | 0.66 | 0.3 |
| | | C1 | 5.0 | 0.99 | −42.4 | 0.98 | | |
| KUV 00311−1938 | 0031−196 | Core | 25.8 | ... | ... | 0.10 | 0.74 | 4.3 |
| | | C2 | 2.7 | 2.55 | 29.9 | 1.39 | | |
| | | C1 | 2.6 | 4.56 | 22.7 | 3.54 | | |
| 1ES 0033+595 | 0033+595 | Core | 43.7 | ... | ... | 0.23 | 0.72 | 1.5 |
| | | C2 | 9.7 | 1.18 | −24.1 | 1.16 | | |
| | | C1 | 5.1 | 5.52 | 69.1 | 4.30 | | |
| RGB J0136+391 | 0133+388 | Core | 28.7 | ... | ... | 0.00 | 0.75 | ... |
| | | C3 | 6.8 | 0.36 | −7.9 | 0.52 | | |
| | | C2 | 2.3 | 0.97 | −59.6 | 1.92 | | |
| | | C1 | 2.5 | 7.99 | −92.4 | 9.45 | | |
| RGB J0152+017 | 0150+015 | Core | 42.6 | ... | ... | 0.16 | 0.80 | 2.9 |
| | | C2 | 4.8 | 1.02 | −135.6 | 0.68 | | |
| | | C1 | 2.9 | 3.27 | −125.4 | 1.61 | | |
| 1ES 0229+200 | 0229+200 | Core | 19.9 | ... | ... | 0.10 | 0.74 | 3.6 |
| | | C4 | 2.2 | 0.94 | 163.6 | 0.50 | | |
| | | C3 | 2.3 | 3.06 | 154.6 | 1.04 | | |
| | | C2 | 1.4 | 6.71 | 160.8 | 2.80 | | |
| | | C1 | 2.4 | 15.76 | 171.6 | 8.79 | | |
| RBS 0413 | 0317+185 | Core | 16.7 | ... | ... | 0.08 | 0.74 | 4.5 |
| | | C3 | 2.6 | 0.85 | −13.9 | 0.38 | | |
| | | C2 | 1.1 | 2.12 | −14.8 | 0.70 | | |
| | | C1 | 1.2 | 5.03 | −11.2 | 1.53 | | |
| 1ES 0347−121 | 0347−121 | Core | 7.4 | ... | ... | 0.14 | 0.89 | 0.6 |
| | | C1 | 1.6 | 1.74 | −144.2 | 1.38 | | |
| 1ES 0414+009 | 0414+009 | Core | 35.7 | ... | ... | 0.28 | 0.78 | 0.8 |
| | | C1 | 11.1 | 1.41 | 85.7 | 2.59 | | |
| 1ES 0502+675 | 0502+675 | Core | 17.2 | ... | ... | 0.26 | 0.75 | 0.4 |
| | | C2 | 2.9 | 0.37 | −139.0 | 0.41 | | |
| | | C1 | 3.2 | 4.58 | −74.5 | 6.90 | | |
| PKS 0548−322 | 0548−322 | Core | 20.4 | ... | ... | 0.32 | 0.69 | 0.3 |
| | | C1 | 6.2 | 1.27 | 30.9 | 0.61 | | |
| RX J0648.7+1516 | 0645+153 | Core | 33.7 | ... | ... | 0.00 | 0.76 | ... |
| | | C5 | 3.9 | 0.81 | −1.9 | 0.32 | | |
| | | C4 | 2.1 | 2.43 | −1.6 | 0.87 | | |
| | | C3 | 1.1 | 4.67 | −10.9 | 2.08 | | |
| | | C2 | 2.6 | 10.77 | −1.3 | 5.09 | | |
| | | C1 | 3.3 | 21.51 | 5.6 | 7.18 | | |
| 1ES 0647+250 | 0647+251 | Core | 41.6 | ... | ... | 0.15 | 0.76 | 3.2 |
| | | C2 | 9.1 | 0.91 | 157.9 | 1.78 | | |
| | | C1 | 1.8 | 3.28 | −82.6 | 3.29 | | |
| RGB J0710+591 | 0706+592 | Core | 27.0 | ... | ... | 0.17 | 0.75 | 1.5 |
| | | C3 | 4.8 | 0.80 | −145.3 | 0.63 | | |
| | | C2 | 3.8 | 3.10 | −156.0 | 1.83 | | |
| | | C1 | 4.9 | 14.50 | −156.7 | 10.57 | | |
| 1RXS J101015.9−311909 | 1008−310 | Core | 30.1 | ... | ... | 0.29 | 0.65 | 0.6 |
| | | C1 | 5.1 | 0.91 | 32.7 | 2.01 | | |
| MS 1221.8+2452 | 1221+248 | Core | 16.0 | ... | ... | 0.22 | 0.68 | 0.6 |
| | | C2 | 2.6 | 0.77 | −129.5 | 0.65 | | |
| | | C1 | 1.6 | 2.15 | −139.0 | 1.12 | | |
| 1ES 1440+122 | 1440+122 | Core | 16.7 | ... | ... | 0.00 | 0.67 | ... |
| | | C3 | 2.5 | 0.48 | −49.6 | 0.42 | | |
| | | C2 | 1.5 | 1.68 | −71.8 | 1.47 | | |
| | | C1 | 1.3 | 12.41 | −81.6 | 6.59 | | |
| H 1722+119 | 1722+119 | Core | 62.5 | ... | ... | 0.00 | 0.68 | ... |
| | | C2 | 3.7 | 0.58 | 152.4 | 0.00 | | |
| | | C1 | 4.0 | 3.50 | 163.3 | 4.29 | | |
| 1ES 1741+196 | 1741+196 | Core | 94.8 | ... | ... | 0.24 | 0.78 | 2.9 |
| | | C3 | 22.0 | 0.75 | 70.0 | 0.67 | | |
| | | C2 | 17.5 | 2.08 | 71.7 | 1.50 | | |
| | | C1 | 7.0 | 6.00 | 81.1 | 2.43 | | |
| B3 2247+381 | 2247+381 | Core | 39.8 | ... | ... | 0.16 | 0.75 | 2.7 |
| | | C3 | 10.3 | 0.69 | −91.5 | 1.53 | | |
| | | C2 | 3.4 | 4.63 | −74.6 | 1.70 | | |
| | | C1 | 1.7 | 9.61 | −59.7 | 3.65 | | |

**Notes.** Column 4: flux density in millijanskys. Columns 5 and 6: $r$ and P.A. are the polar coordinates of the center of the component relative to the presumed core. Position angle is measured from north through east. Column 7: FWHM of the Gaussian component. Column 8: the reduced chi-squared of the model fit. Column 9: the maximum observer-frame brightness temperature of the Gaussian core component is given by $T_B = 1.22 \times 10^{12} S/(a^2 \nu^2)$ K, where $S$ is the flux density in janskys, $a$ is the FWHM in milliarcseconds, and $\nu$ is the observation frequency in GHz. Brightness temperature is given for core components for which the best-fit size is not zero.

**Table 5**
Brightness Temperature Error Analysis

| B1950 Name | $S$ (mJy) | $a$ (mas) | $T_B$ ($10^{10}$ K) | $S_{\max}$ (mJy) | $a_{\min}$ (mas) | $T_{B,\max}$ ($10^{10}$ K) | $S_{\min}$ (mJy) | $a_{\max}$ (mas) | $T_{B,\min}$ ($10^{10}$ K) |
|---|---|---|---|---|---|---|---|---|---|
| (1) | (2) | (3) | (4) | (5) | (6) | (7) | (8) | (9) | (10) |
| 0011−191 | 9.3 | 0.23 | 0.3 | 13.4 | 0.00 | ∞ | 7.1 | 0.36 | 0.1 |
| 0031−196 | 25.8 | 0.10 | 4.3 | 29.3 | 0.00 | ∞ | 22.3 | 0.19 | 1.1 |
| 0033+595 | 43.7 | 0.23 | 1.5 | 48.2 | 0.14 | 4.4 | 39.2 | 0.30 | 0.8 |
| 0133+388 | 28.7 | 0.00 | ∞ | 33.3 | 0.00 | ∞ | 22.3 | 0.27 | 0.5 |
| 0150+015 | 42.6 | 0.16 | 2.9 | 45.1 | 0.09 | 10.3 | 38.1 | 0.23 | 1.3 |
| 0229+200 | 19.9 | 0.10 | 3.6 | 23.4 | 0.00 | ∞ | 16.4 | 0.23 | 0.5 |
| 0317+185 | 16.7 | 0.08 | 4.5 | 19.2 | 0.00 | ∞ | 14.2 | 0.22 | 0.5 |
| 0347−121 | 7.4 | 0.14 | 0.6 | 10.9 | 0.00 | ∞ | 4.9 | 0.28 | 0.1 |
| 0414+009 | 35.7 | 0.28 | 0.8 | 40.2 | 0.17 | 2.4 | 32.2 | 0.33 | 0.5 |
| 0502+675 | 17.2 | 0.26 | 0.4 | 22.7 | 0.11 | 3.1 | 13.7 | 0.37 | 0.2 |
| 0548−322 | 20.4 | 0.32 | 0.3 | 26.9 | 0.12 | 3.0 | 15.9 | 0.36 | 0.2 |
| 0645+153 | 33.7 | 0.00 | ∞ | 39.0 | 0.00 | ∞ | 30.0 | 0.21 | 1.2 |
| 0647+251 | 41.6 | 0.15 | 3.2 | 45.1 | 0.10 | 8.2 | 38.1 | 0.23 | 1.2 |
| 0706+592 | 27.0 | 0.17 | 1.5 | 31.5 | 0.00 | ∞ | 22.5 | 0.29 | 0.5 |
| 1008−310 | 30.1 | 0.29 | 0.6 | 37.6 | 0.13 | 3.9 | 24.6 | 0.39 | 0.3 |
| 1221+248 | 16.0 | 0.22 | 0.6 | 20.5 | 0.00 | ∞ | 12.5 | 0.34 | 0.2 |
| 1440+122 | 16.7 | 0.00 | ∞ | 20.2 | 0.00 | ∞ | 13.2 | 0.23 | 0.4 |
| 1722+119 | 62.5 | 0.00 | ∞ | 65.9 | 0.00 | ∞ | 58.9 | 0.13 | 6.0 |
| 1741+196 | 94.8 | 0.24 | 2.9 | 98.0 | 0.21 | 3.8 | 89.2 | 0.28 | 1.9 |
| 2247+381 | 39.8 | 0.16 | 2.7 | 44.3 | 0.00 | ∞ | 35.3 | 0.23 | 1.1 |

**Notes.** Columns 2–4 are the best-fit core flux density and size and the associated observer-frame brightness temperature. These values are also given in Table 4. Columns 5–7 are the maximum allowed core flux density and the minimum allowed size, and the associated maximum brightness temperature computed from those quantities. Columns 8–10 are the minimum allowed core flux density and the maximum allowed size, and the associated minimum brightness temperature computed from those quantities.

Care must be taken in the analysis of these VLBI core brightness temperatures because many of the cores are only partially resolved, and even though a best-fit size may be returned by the model fitting routine, the fit is often nearly as good if the Gaussian component is simply replaced by a delta function. In such cases, only an upper limit to the size, or a lower limit to the brightness temperature, can actually be measured. The flux density of the core and the baseline lengths and sensitivity of the VLBI array determine the maximum measurable brightness temperature (e.g., Lovell et al. 2000; Wehrle et al. 2001; Kovalev et al. 2005; Lobanov 2005), which is of order $10^{11}$ K for these observations. Because some core brightness temperatures in Table 4 are within factors of a few of this value, we conducted a full error analysis of the core brightness temperatures; this error analysis is described below and tabulated in Table 5.

We used the Difwrap program (Lovell 2000), as described by, e.g., Piner et al. (2000) and Tingay et al. (2001), to determine upper and lower bounds to the measured brightness temperatures. We established minimum and maximum values for the flux density and size of a component by systematically varying that property, while allowing other parameters to reconverge, and then visually comparing the new fit to the measured visibilities. The upper bound to the brightness temperature was then computed using the maximum flux and the minimum size, and the lower bound to the brightness temperature was computed using the minimum flux and the maximum size. All of these values are tabulated in Table 5.

Roughly half of the core components are consistent with a size of zero, meaning that the associated brightness temperature measurements have no upper bound and are only lower limits, but the half that do have upper bounds provide valuable constraints. If we exclude the single high-brightness temperature source 1722+119 ($T_B > 6.0 \times 10^{10}$ K), then the largest lower limit is $T_B > 1.9 \times 10^{10}$ K for 1741+196. Similarly, the smallest upper limit is $T_B < 2.4 \times 10^{10}$ K for 0414+009. Thus, all except one of these 20 sources are consistent with the brightness temperature range $1.9 \times 10^{10} < T_B < 2.4 \times 10^{10}$ K, and we therefore take a brightness temperature of $\sim 2 \times 10^{10}$ K to be a typical observed brightness temperature of a TeV HBL. This is consistent with typical observed brightness temperatures of TeV HBLs measured in earlier works (e.g., Piner et al. 2010), but it is now established for a much larger number of sources. To compare with intrinsic brightness temperature limits that have been derived for homogeneous optically thick spheres, we can convert our Gaussian brightness temperatures to homogeneous sphere brightness temperatures by multiplying by the appropriate correction factor of 0.56 (e.g., Pearson 1995; Tingay et al. 2001). This yields a value of about $1 \times 10^{10}$ K as a typical brightness temperature of a TeV HBL.

Comparing the typical observed brightness temperatures to the equipartition brightness temperatures calculated for these sources of about $6 \times 10^{10}$ K (Equation (4a) of Readhead 1994), we see that the observed brightness temperatures of these TeV HBLs are already at or below the equipartition limit with no need to invoke high Doppler factors to reduce the observed brightness temperatures. There is thus no evidence of relativistic beaming of the core emission based on the VLBI brightness temperatures. Even with no Doppler boosting, the observed brightness temperatures are already somewhat below the equipartition value, placing these sources in the magnetically dominated regime (Readhead 1994; Homan et al. 2006). High values of the Doppler factor would reduce the intrinsic brightness temperature even more, placing the sources even farther from equipartition. We note one important caveat: both observed brightness temperatures and intrinsic physical limits are traditionally calculated for a homogeneous sphere geometry, and the actual geometry for the VLBI core region may be more complex, such as a partially resolved limb-brightened structure (see Section 3.5).

Despite the lack of evidence for beaming from the VLBI brightness temperatures, the one-sided core-jet morphology displayed by the majority of these sources does imply at least mild Doppler boosting. However, because the sources studied in this paper are relatively faint, this constraint is modest. We have computed lower limits to the jet-to-counterjet brightness ratio for each source, based on the peak jet brightness from the model fits in Table 4, restored with the associated beam from Table 3, and using three times the rms noise from Table 3 as the minimum detectable counterjet brightness. The median lower limit to the jet-to-counterjet brightness ratio is 37:1, which implies $\delta > 2$ for viewing angles of a few degrees. The highest lower limit is 210:1 for 1741+196, which implies $\gamma > 2$ and $\delta > 4$ for viewing angles of a few degrees.

### 3.4. Opening Angles

We have calculated the apparent opening angle $\phi_{\rm app}$ of each of these 20 jets, using the model fits from Table 4 and the model-fitting approach to measuring apparent opening angles described by Pushkarev et al. (2009). These apparent opening angles are tabulated in Table 6. Note that the apparent opening angle is a function of both the intrinsic opening angle and the viewing angle through the relation $\phi_{\rm app} \approx \phi_{\rm int} / \sin\theta$, where $\theta$ is the viewing angle. Pushkarev et al. (2009) compared apparent

**Table 6**
Apparent Opening Angles

| B1950 Name | $\phi_{app}$ (deg) | B1950 Name | $\phi_{app}$ (deg) | B1950 Name | $\phi_{app}$ (deg) | B1950 Name | $\phi_{app}$ (deg) |
|---|---|---|---|---|---|---|---|
| 0011−191 | 26.2 | 0229+200 | 13.0 | 0548−322 | 13.4 | 1221+248 | 18.9 |
| 0031−196 | 18.2 | 0317+185 | 10.2 | 0645+153 | 11.3 | 1440+122 | 20.7 |
| 0033+595 | 23.8 | 0347−121 | 21.6 | 0647+251 | 35.5 | 1722+119 | 31.5 |
| 0133+388 | 37.2 | 0414+009 | 42.6 | 0706+592 | 19.3 | 1741+196 | 18.4 |
| 0150+015 | 16.2 | 0502+675 | 33.1 | 1008−310 | 47.8 | 2247+381 | 23.0 |

opening angles of *Fermi*-detected and nondetected blazars and found a tendency for the *Fermi*-detected blazars to have wider apparent opening angles than the nondetected ones. Because the calculated intrinsic opening angles of the two groups were similar, they suggested that the *Fermi*-detected jets were viewed more closely to the line of sight. Lister et al. (2011) used a larger sample of *Fermi*-detected blazars to compute a mean apparent opening angle of 24° for this sample, and they also found a positive correlation between apparent opening angle and the gamma-ray loudness of the source.

The apparent opening angles in Table 6 range from 10° to 48°, with a mean of 24° ± 2°, identical to the mean found by Lister et al. (2011) for a larger sample of *Fermi*-detected blazars. Because 16 out of 20 of the TeV sources imaged for this paper are also *Fermi* sources (see Table 7), this identical mean is not surprising, but it does show that the apparent opening angle distribution for a TeV HBL selected subset of *Fermi* sources is similar to the overall *Fermi*-detected distribution. There is thus no evidence from apparent opening angles that TeV HBLs have different distributions of either viewing angle or intrinsic opening angle compared to the larger sample of *Fermi* sources studied by Lister et al. (2011). We find no significant correlation between the apparent opening angles in Table 6 and TeV gamma-ray loudness (see Section 4.3) as was found by Lister et al. (2011); however, this is not conclusive considering our small sample size of 20 sources.

### 3.5. Morphology and Transverse Jet Structure

AGN jets may be expected to develop transverse (so-called spine-sheath or spine-layer) velocity structures on theoretical grounds (e.g., Henri & Pelletier 1991), and the existence of these structures could explain some important observed properties of the TeV HBLs. For example, Ghisellini et al. (2005) consider how a jet with a low Lorentz factor layer and a high Lorentz factor spine could produce the discrepant Lorentz factors that are observed for TeV HBLs in the radio and gamma-ray, while at the same time the interaction between these two regions could serve to decelerate the spine. Recently, Tavecchio et al. (2014) calculated whether spine-layer structures in the TeV HBLs could also produce high-energy PeV neutrinos, such as those detected by IceCube (Aartsen et al. 2014).

Such spine-sheath structures might produce limb brightening in the VLBI images of these jets if, for example, the jet bends away from the line of sight such that the low Lorentz factor layer acquires a higher Doppler factor than the high Lorentz factor spine (e.g., Giroletti et al. 2004a) or if the layer simply has a higher synchrotron emissivity in the radio than the spine (e.g., Sahayanathan 2009; Ghisellini et al. 2005). Note though that the presence of transverse intensity structures in VLBI images can have causes other than two-component outflows; for example, Clausen-Brown et al. (2011) show that limb brightening can be observed for a uniform cylindrical jet with a helical magnetic field and no transverse structure under certain viewing geometries.

Limb brightening has been observed a number of times in VLBI images of two of the brightest and closest TeV HBLs: Mrk 421 and Mrk 501. Giroletti et al. (2004a, 2008), Piner et al. (2009), and Croke et al. (2010) have all reported limb brightening in VLBI images of Mrk 501 at a wide variety of distances from the core. Similar results have been obtained for Mrk 421, both at lower frequencies (Giroletti et al. 2006) and at 43 GHz (Piner et al. 2010; Blasi et al. 2013). Transverse polarization structures, both in electric vector position angle (EVPA) and fractional polarization, have also been observed in both of these sources, as well as in the TeV HBL 1ES 1959+650 (Piner et al. 2010).

We have produced transverse brightness profiles for all 20 of the sources imaged for this paper at numerous points along their jets. Many of these sources display the following general pattern in their transverse structure: the jets are well collimated and unresolved in the transverse direction for the first few milliarcseconds, after which they transition to a patchy low surface brightness emission that is resolved but has numerous intensity peaks in a transverse brightness profile. Of the 20 sources, we see only two examples of a classic limb-brightening profile, in the sources 0502+675 and 1722+119. Transverse brightness profiles showing the limb brightening for these two sources are shown in Figure 2; the limb-brightened structure of these two sources can also be seen directly on the images shown in Figure 1. For both of these sources, the limb brightening remains visible over a radial range of roughly 3 mas.

We note that the absence of such a clear signature of limb brightening in the other sources does not mean that such transverse intensity structure is nonexistent in these jets. For example, the observations of limb brightening by Piner et al. (2009) and Piner et al. (2010) in the relatively nearby TeV HBLs Mrk 501 and Mrk 421 were obtained from high-resolution 43 GHz observations, after subtraction of the core and super-resolution of the jet in the transverse direction. That same linear scale would correspond to an angular separation that is well within the jet region that is transversely unresolved in the lower-resolution 8 GHz images of the more distant TeV HBLs presented in this paper. It is possible that the inner jets of these sources would display such structures if they could be transversely resolved with high-frequency VLBI; unfortunately, observations at high frequency are much less sensitive, and all but the brightest few TeV HBLs are too faint for this. Whether spine-sheath structures are a nearly universal structure for TeV HBL jets is therefore ambiguous from these observations.

## 4. RESULTS FOR THE ENTIRE TeV HBL SAMPLE

### 4.1. VLBI and Gamma-Ray Data for the Sample

In this section, we combine the new VLBI data obtained in this paper with gamma-ray and VLBI data on the other TeV HBLs. The VLBI and gamma-ray properties of the 44 TeV HBLs currently listed in the TeVCat catalog are tabulated in Table 7. We have attempted to quote a redshift value for every source in Table 7, but in a number of cases (9 out of 44) these values are either uncertain or they are lower limits. These cases are clearly indicated in the notes to Table 7, and those values should be used with caution.

About half of the VLBI data in Table 7 (20 sources) comes from this paper; VLBI data for most of the other HBLs comes from either our prior publications (13 sources), or from the

**Table 7**
VLBI and Gamma-Ray Properties of the TeV HBLs

| Source | $z$ | $\nu$ (GHz) | VLBI Total (mJy) | VLBI Core (mJy) | $T_B$ ($10^{10}$K) | Ref | TeV Flux (Crab) | TeV Flux ($10^{-12}$ photon cm$^{-2}$ s$^{-1}$) | Cutoff (TeV) | Ind | Ref | *Fermi* Flux ($10^{-12}$ erg cm$^{-2}$ s$^{-1}$) | Ind | Log $G_{\rm TeV}$ | $\overline{m}$ |
|---|---|---|---|---|---|---|---|---|---|---|---|---|---|---|---|
| (1) | (2) | (3) | (4) | (5) | (6) | (7) | (8) | (9) | (10) | (11) | (12) | (13) | (14) | (15) | (16) |
| SHBL J001355.9−185406 | 0.095 | 8.4 | 15 | 9 | 0.3 | 1 | 0.006 | 0.8 | 0.31 | 3.40 | 1 | ... | ... | 2.89 | ... |
| KUV 00311−1938 | 0.506[a] | 8.4 | 31 | 26 | 4.3 | 1 | 0.010 | 1.2[a] | 0.33 | 3.70 | 2 | 40.0 | 1.76 | 3.17 | ... |
| 1ES 0033+595 | 0.240[a] | 8.4 | 59 | 44 | 1.5 | 1 | 0.015 | 5.5[b] | 0.15 | 3.80 | 3,4 | 28.6 | 1.87 | 2.36 | ... |
| RGB J0136+391 | 0.400[a] | 8.4 | 40 | 29 | ur | 1 | ... | ...[c] | ... | ... | 4 | 61.9 | 1.69 | ... | ... |
| RGB J0152+017 | 0.080 | 8.4 | 51 | 43 | 2.9 | 1 | 0.020 | 2.7 | 0.30 | 2.95 | 5 | 9.6 | 1.79 | 2.88 | ... |
| 1ES 0229+200 | 0.140 | 8.4 | 28 | 20 | 3.6 | 1 | 0.017 | 2.3 | 0.30 | 2.59 | 6 | ... | ... | 3.19 | ... |
| PKS 0301−243 | 0.266 | 15.4 | 218 | 157 | 5.2 | 2 | 0.014 | 3.3 | 0.20 | 4.60 | 7 | 76.6 | 1.94 | 1.83 | ... |
| IC 310 | 0.019 | 15.4 | 102 | 62 | 2.0 | 2 | 0.023 | 3.1 | 0.30 | 2.00 | 8 | 9.8 | 2.10 | 2.86 | ... |
| RBS 0413 | 0.190 | 8.4 | 22 | 17 | 4.5 | 1 | 0.009 | 1.5 | 0.25 | 3.18 | 9 | 17.0 | 1.55 | 2.88 | ... |
| 1ES 0347−121 | 0.188 | 8.4 | 9 | 7 | 0.6 | 1 | 0.022 | 3.9 | 0.25 | 3.10 | 10 | ... | ... | 3.67 | ... |
| 1ES 0414+009 | 0.287 | 8.4 | 49 | 36 | 0.8 | 1 | 0.021 | 5.2 | 0.20 | 3.40 | 11 | 7.8 | 1.98 | 2.88 | ... |
| PKS 0447−439 | 0.200[b] | ... | ... | ... | ... | ... | 0.027 | 4.7 | 0.25 | 3.89 | 12 | 135.6 | 1.86 | ... | ... |
| 1ES 0502+675 | 0.314[c] | 8.4 | 23 | 17 | 0.4 | 1 | 0.060 | 8.1[b] | 0.30 | 3.92 | 13 | 42.3 | 1.49 | 3.85 | ... |
| PKS 0548−322 | 0.069 | 8.4 | 27 | 20 | 0.3 | 1 | 0.015 | 2.7 | 0.25 | 2.86 | 14 | ... | ... | 3.01 | ... |
| RX J0648.7+1516 | 0.179 | 8.4 | 43 | 34 | ur | 1 | 0.033 | 8.1[a] | 0.20 | 4.40 | 15 | 20.4 | 1.74 | 2.85 | ... |
| 1ES 0647+250 | 0.450 | 8.4 | 53 | 42 | 3.2 | 1 | 0.030 | 19.5[b] | 0.10 | ... | 16 | 27.2 | 1.59 | 2.91 | ... |
| RGB J0710+591 | 0.125 | 8.4 | 40 | 27 | 1.5 | 1 | 0.029 | 3.9 | 0.30 | 2.69 | 17 | 13.3 | 1.53 | 3.23 | 0.064 |
| 1ES 0806+524 | 0.138 | 22.2 | 89 | 64 | 0.9 | 3 | 0.016 | 2.2 | 0.30 | 3.60 | 18 | 27.9 | 1.94 | 2.53 | 0.120 |
| RBS 0723 | 0.198 | 8.4 | 6 | 6 | ... | 4 | 0.025 | 6.1[b] | 0.20 | ... | 19 | 9.3 | 1.48 | 3.83 | ... |
| 1RXS J101015.9−311909 | 0.143 | 8.4 | 35 | 30 | 0.6 | 1 | 0.010 | 2.4 | 0.20 | 3.08 | 20 | 9.8 | 2.24 | 2.64 | ... |
| 1ES 1011+496 | 0.212 | 15.4 | 191 | 106 | 2.5 | 3 | 0.065 | 15.8 | 0.20 | 4.00 | 21 | 72.6 | 1.85 | 2.59 | ... |
| 1ES 1101−232 | 0.186 | 8.4 | 28 | 23 | 0.6 | 5 | 0.019 | 4.5 | 0.20 | 2.94 | 22 | 6.1 | 1.80 | 3.10 | ... |
| Markarian 421 | 0.031 | 8.6 | 421 | 285 | 25.6 | 6 | 0.645 | 156.7[d] | 0.20 | 2.20 | 23 | 375.7 | 1.77 | 3.71 | 0.083 |
| Markarian 180 | 0.045 | 22.2 | 83 | 40 | 7.6 | 5 | 0.093 | 22.5 | 0.20 | 3.30 | 24 | 14.9 | 1.74 | 3.10 | 0.094 |
| RX J1136.5+6737 | 0.134 | 8.4 | 23 | 19 | ur | 7 | 0.015 | 3.6[b] | 0.20 | ... | 25 | 8.4 | 1.68 | 2.97 | ... |
| 1ES 1215+303 | 0.130 | 15.4 | 295 | 224 | ur | 2 | 0.032 | 7.7 | 0.20 | 2.96 | 26 | 61.2 | 2.02 | 2.26 | 0.087 |
| 1ES 1218+304 | 0.184 | 8.4 | 39 | 24 | 1.5 | 5 | 0.050 | 12.2 | 0.20 | 3.08 | 27 | 37.8 | 1.71 | 3.34 | ... |
| MS 1221.8+2452 | 0.218 | 8.4 | 21 | 16 | 0.6 | 1 | 0.040 | 9.7[b] | 0.20 | ... | 28 | 7.0 | 2.03 | 3.50 | ... |
| 1ES 1312−423 | 0.105 | ... | ... | ... | ... | ... | 0.007 | 1.1[a] | 0.28 | 2.85 | 29 | ... | ... | ... | ... |
| PKS 1424+240 | 0.604[a] | 15.4 | 218 | 123 | 6.1 | 2 | 0.042 | 21.0 | 0.12 | 3.80 | 30 | 145.0 | 1.78 | 2.41 | 0.069 |
| H 1426+428 | 0.129 | 8.4 | 22 | 19 | 1.1 | 8 | 0.136 | 20.4 | 0.28 | 3.55 | 31 | 16.8 | 1.32 | 4.02 | ... |
| 1ES 1440+122 | 0.163 | 8.4 | 22 | 17 | ur | 1 | 0.010 | 2.4[b] | 0.20 | 3.40 | 13 | 8.9 | 1.41 | 2.79 | ... |
| PG 1553+113 | 0.500[d] | 22.2 | 134 | 95 | 1.2 | 5 | 0.080 | 29.3[b] | 0.15 | 4.27 | 32 | 197.4 | 1.67 | 2.87 | 0.082 |
| Markarian 501 | 0.034 | 8.3 | 902 | 476 | 51.9 | 9 | 0.229 | 31.1[d] | 0.30 | 2.72 | 33 | 114.4 | 1.74 | 2.70 | 0.037 |
| H 1722+119 | 0.170[a] | 8.4 | 70 | 63 | ur | 1 | 0.020 | 8.1[b] | 0.14 | ... | 34 | 42.3 | 1.93 | 2.52 | 0.114 |
| 1ES 1727+502 | 0.055 | 15.4 | 101 | 68 | 5.8 | 2 | 0.021 | 7.7[b] | 0.15 | 3.20 | 35,4 | 9.7 | 1.83 | 2.31 | ... |
| 1ES 1741+196 | 0.083 | 8.4 | 145 | 95 | 2.9 | 1 | 0.008 | 1.4[b] | 0.25 | ... | 36 | 9.4 | 1.62 | 1.93 | ... |
| HESS J1943+213 | 0.140[e] | 1.6 | 31 | 31 | 0.006 | 10 | 0.018 | 1.3 | 0.47 | 3.10 | 37 | ... | ... | 3.21 | ... |
| 1ES 1959+650 | 0.047 | 15.4 | 150 | 91 | 2.3 | 11 | 0.146 | 19.8 | 0.30 | 2.72 | 38 | 66.9 | 1.94 | 3.30 | 0.115 |
| PKS 2005−489 | 0.071 | 8.6 | 461 | 454 | 1.6 | 7 | 0.029 | 2.6 | 0.40 | 3.20 | 39 | 48.1 | 1.78 | 2.13 | ... |
| PKS 2155−304 | 0.116 | 15.4 | 181 | 139 | 2.2 | 11 | 0.178 | 43.2 | 0.20 | 3.53 | 40 | 282.8 | 1.84 | 3.05 | ... |
| B3 2247+381 | 0.119 | 8.4 | 55 | 40 | 2.7 | 1 | 0.021 | 5.0 | 0.20 | 3.20 | 41 | 13.2 | 1.84 | 2.72 | ... |
| 1ES 2344+514 | 0.044 | 15.4 | 118 | 87 | 5.4 | 11 | 0.078 | 10.6 | 0.30 | 2.78 | 42 | 20.6 | 1.72 | 3.11 | ... |
| H 2356−309 | 0.165 | 8.4 | 24 | 17 | 4.4 | 5 | 0.016 | 3.1 | 0.24 | 3.06 | 43 | 7.1 | 1.89 | 3.10 | ... |

**Notes.** Column 1: canonical name from TeVCat; column 2: redshift; column 3: VLBI observing frequency; column 4: total VLBI flux density; column 5: VLBI core flux density; column 6: core observer-frame Gaussian brightness temperature (ur = unresolved); column 7: reference for VLBI data; column 8: integrated TeV photon flux above the cutoff energy in multiples of the Crab flux; column 9: integrated TeV photon flux above the cutoff energy; column 10: cutoff energy for TeV flux; column 11: TeV photon spectral index; column 12: reference for TeV data; columns 13 and 14: 2FGL *Fermi* energy flux and photon spectral index; column 15: log TeV loudness (see Section 4.3); column 16: intrinsic modulation index from Richards et al. (2014; see Section 4.5).

**Notes for Column 2.** [a]: value is a lower limit. [b]: uncertain. Value used is from Prandini et al. 2012. [c]: uncertain. Value used is from NASA/IPAC Extragalactic Database but is controversial. [d]: range 0.43–0.58. We use the mean. [e]: value is a lower limit, but nature of source is controversial. See discussion later in text.

**Notes for Column 9.** [a]: computed from a differential flux from the reference. [b]: computed from a flux in Crabs from the reference. [c]: positive detection reported, no other information. [d]: mean value computed from multiple fluxes in the reference.

**References for Column 7.** (1) This paper; (2) MOJAVE program; (3) Piner & Edwards 2013; (4) Bourda et al. 2010; (5) Tiet et al. 2012; (6) Piner et al. 2012; (7) http://astrogeo.org/; (8) Piner et al. 2008; (9) Piner et al. 2007; (10) Gabányi et al. 2013; (11) Piner & Edwards 2004.

**References for Column 12.** (1) Abramowski et al. 2013a; (2) Becherini et al. 2012; (3) Mariotti 2011; (4) Mazin 2012; (5) Aharonian et al. 2008; (6) Aliu et al. 2014; (7) Abramowski et al. 2013b; (8) Aleksić et al. 2010; (9) Aliu et al. 2012a; (10) Aharonian et al. 2007a; (11) Aliu et al. 2012b; (12) Abramowski et al. 2013d; (13) Benbow 2011; (14) Aharonian et al. 2010; (15) Aliu et al. 2011; (16) De Lotto 2012; (17) Acciari et al. 2010; (18) Acciari et al. 2009a; (19) Mirzoyan 2014a; (20) Abramowski et al. 2012; (21) Albert et al. 2007a; (22) Aharonian et al. 2007b; (23) Albert et al. 2007b; (24) Albert et al. 2006a; (25) Mirzoyan 2014b; (26) Aleksić et al. 2012a; (27) Acciari et al. 2009b; (28) Cortina 2013a; (29) Abramowski et al. 2013c (30) Archambault et al. 2014; (31) Horan et al. 2002; (32) Aleksić et al. 2012b; (33) Acciari et al. 2011b; (34) Cortina 2013b; (35) Aleksić et al. 2014b; (36) Berger 2011; (37) Abramowski et al. 2011; (38) Albert et al. 2006b; (39) Acero et al. 2010; (40) Abramowski et al. 2010a; (41) Aleksić et al. 2012c; (42)Acciari et al. 2011a; (43) Abramowski et al. 2010b.

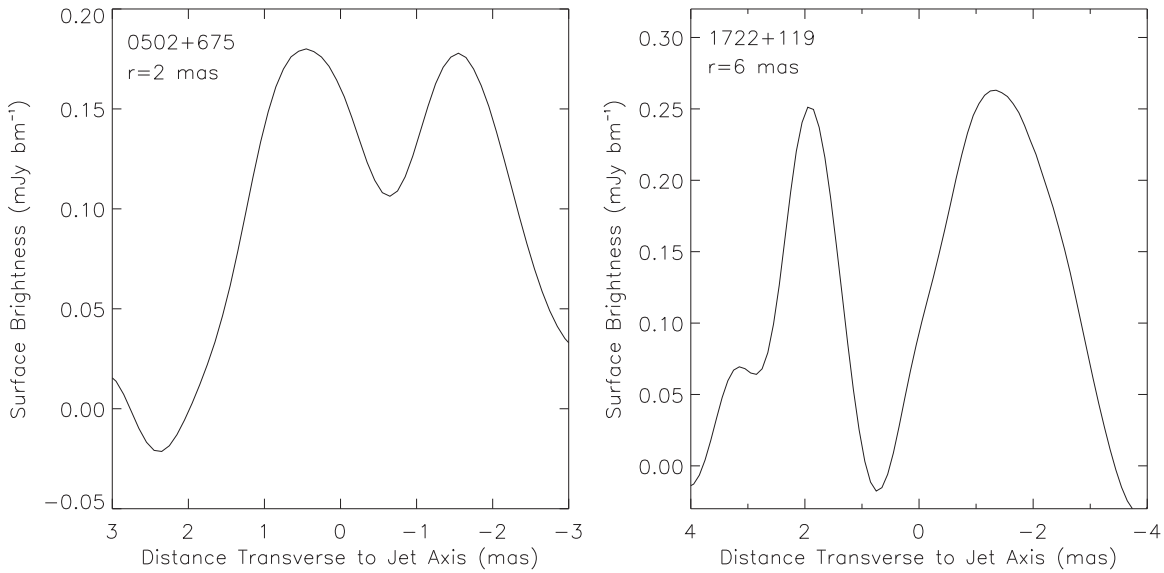


**Figure 2.** Transverse brightness profiles showing limb brightening for 0502+675 at 2 mas from the core (left panel) and for 1722+119 at 6 mas from the core (right panel). The rms noise levels (or uncertainty on the curves) are 0.023 mJy bm$^{-1}$ for 0502+675 and 0.030 mJy bm$^{-1}$ for 1722+119 (see Table 3).

MOJAVE program (five sources). Four sources have VLBI data taken from elsewhere in the literature. Only two of the 44 sources (both below −40° declination) have no VLBI data in the literature. All of the VLBI data taken from elsewhere, such as that taken from the MOJAVE survey, has been independently model-fit by us if the visibility data files were available online; if not, then published values have been used. For sources with multiple epochs of VLBI data, we have model-fit all epochs and then used the epoch having the median core brightness temperature. VLBI data at an observing frequency of 8 GHz (the observing frequency used for this paper) were preferred if they were available; if not, then data at either 15 or 22 GHz (or in a single case, 1.6 GHz) have been used. References for all VLBI data used are given in the notes of Table 7.

The *Fermi* gamma-ray fluxes and spectral indices in Table 7 are taken from the 2FGL catalog (Nolan et al. 2012). Only six of the 44 sources have not been detected by *Fermi*, as of the 2FGL catalog. For the TeV gamma-ray data, an integrated photon flux, cutoff energy for that flux, and spectral index (uncorrected for extragalactic background light (EBL) absorption) was taken from the literature, if available. That integrated photon flux was then independently converted to a multiple of the Crab nebula flux using the Crab spectrum from Aharonian et al. (2006); this may cause slight differences from Crab fluxes quoted in the original papers referenced in Table 7. In some cases, only a flux that was already expressed in multiples of the Crab flux was given in the literature. In those cases, the integrated photon flux above the cutoff energy was calculated from that using the Crab spectrum from Aharonian et al. (2006). For many of the sources, the numbers given in Table 7 match the flux in multiples of the Crab flux, cutoff energy, and spectral index quoted for that source in TeVCat; but in a number of cases they differ, due either to different literature sources used or differing Crab nebula standards. Many of the newly discovered sources have only a single flux value in the literature, but for frequently observed sources, the variability of the TeV HBLs makes selection of a single flux value problematic. Because sources are observed over different time and energy ranges with different instruments, calculation of a formal mean would be difficult. Nevertheless, we have tried to select a typical flux value for variable sources, excluding extreme high or low states. This exclusion of extreme high or low states may also cause the numbers in Table 7 to differ from those in TeVCat. In any event, the TeV data will almost certainly not be contemporaneous with the VLBI measurements. References for all TeV data used are given in the notes to Table 7.

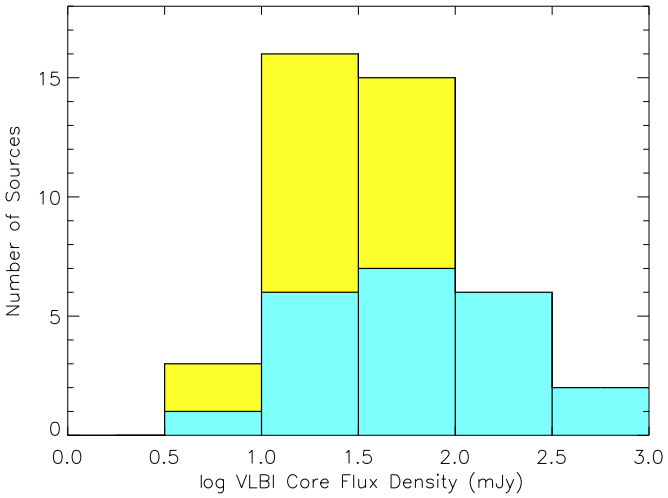


**Figure 3.** Histogram of VLBI core flux densities of TeV HBLs from Table 7. New sources with VLBI data from this paper are shown in yellow (20 sources). Sources with data taken from elsewhere are shown in blue (22 sources).
(A color version of this figure is available in the online journal.)

### *4.2. VLBI Flux Densities and Brightness Temperatures*

A histogram of the VLBI core flux densities of the TeV HBLs from Table 7, which is indicative of the most compact emission from these sources, is shown in Figure 3. New sources with VLBI data from this paper are shown in yellow, and sources with data taken from elsewhere are shown in blue. The range in core flux densities spans from a few millijanskys (e.g., 1ES 0347−121) to a few hundred millijanskys (e.g., Mrk 421 and Mrk 501), with a median of 38 mJy. Note that all of the new sources added in this paper have cores that are under 100 mJy.

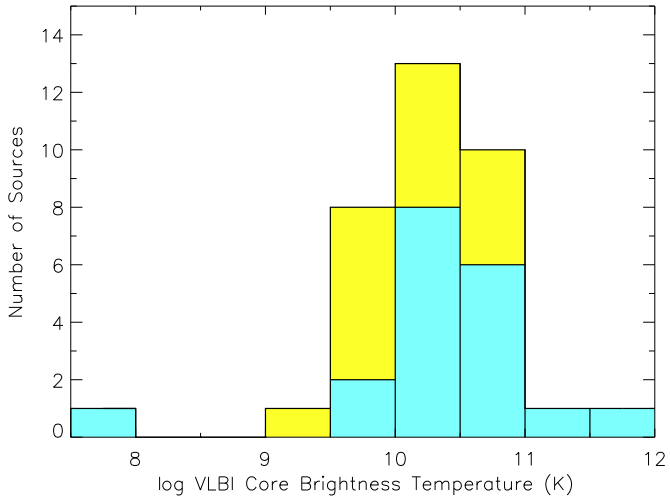


**Figure 4.** Histogram of observer-frame Gaussian core brightness temperatures of TeV HBLs from Table 7, for sources whose best-fit core size is not zero. New sources with VLBI data from this paper are shown in yellow (16 sources). Sources with data taken from elsewhere are shown in blue (19 sources). The outlier is HESS J1943+213 (see text).

(A color version of this figure is available in the online journal.)

As the TeV gamma-ray telescopes have become more sensitive and begun to detect fainter objects, these sources have also tended to be fainter in the radio, a potential correlation that is explored in Section 4.4.

A histogram of the VLBI core brightness temperatures from Table 7 is shown in Figure 4. New sources with VLBI data from this paper are shown in yellow, and sources with data taken from elsewhere are shown in blue. A brightness temperature value has been plotted in Figure 4 unless the best-fit value for the core size is zero (indicated by "ur" in Table 7). However, as indicated by the brightness temperature error analysis done for the 20 sources observed for this paper in Section 3.3, some of these brightness temperature values are probably actually lower limits. The median brightness temperature in Figure 4 is $2 \times 10^{10}$ K, which is the same as the typical brightness temperature obtained from the brightness temperature error analysis in Section 3.3. See Section 3.3 for a discussion of the physical interpretation of such brightness temperatures in terms of intrinsic brightness temperature limits and relativistic beaming.

Some outliers are notable in Figure 4. The only two TeV HBLs with brightness temperatures over $10^{11}$ K are the well-studied sources Mrk 421 and Mrk 501. The low brightness temperature outlier, with a measured brightness temperature of only $6 \times 10^{7}$ K, is the source HESS J1943+213, which lies close to the Galactic plane. This source was observed with the European VLBI Network at 1.6 GHz by Gabányi et al. (2013), who measured it to have a flux density of 31 mJy and an angular size of 16 mas, giving it a brightness temperature two orders of magnitude lower than all other TeV HBLs in Figure 4. The distribution in Figure 4 casts significant doubt on the HBL classification of this object (unless it is affected by an unusually large amount of interstellar scattering; see the discussion in Gabányi et al. 2013), and Gabányi et al. (2013) suggest instead a galactic origin for this source, in the form of a remote pulsar wind nebula. This interpretation may be strengthened by the lack of detection of any significant variability from this object from radio to TeV gamma-rays (Abramowski et al. 2011).

### 4.3. TeV Loudness

In this section, we quantify the distribution of the ratio of TeV gamma-ray to radio luminosity present in the TeV HBL population. Lister et al. (2011) performed a similar analysis for *Fermi*-detected blazars by defining a quantity that they called the gamma-ray loudness, $G_r$. This quantity was defined by Lister et al. (2011) as the ratio of the gamma-ray luminosity between 0.1 GeV and 100 GeV, divided by the radio luminosity over a 15 GHz wide bandwidth, calculated from the VLBA flux density at 15 GHz (see Equations (2)–(4) of Lister et al. 2011). We make straightforward modifications to Equations (2)–(4) of Lister et al. (2011) to adapt their gamma-ray loudness statistic to the TeV energy range and main VLBA observing frequency considered in this paper. We calculate the TeV loudness, $G_{\rm TeV} = L_{\rm TeV}/L_{\rm R}$, using the gamma-ray luminosity between 0.3 and 30 TeV, accounting for the different lower energy thresholds for the different measurements given in Table 7. The modified versions of Equations (2)–(4) from Lister et al. (2011) are

$$S_{\rm TeV} = \frac{(\Gamma-1)C_1 E_0 F_0}{(\Gamma-2)} \left(\frac{E_0}{E_1}\right)^{\Gamma-2} \left[1-\left(\frac{E_1}{E_2}\right)^{\Gamma-2}\right] \ {\rm erg\,cm^{-2}\,s^{-1}}, \quad (2)$$

where $F_0$ is the measured photon flux above the cutoff energy $E_0$, $\Gamma$ is the photon spectral index, $E_1 = 0.3$ TeV, $E_2 = 30$ TeV, and $C_1 = 1.602\,{\rm erg\,TeV^{-1}}$,

$$L_{\rm TeV} = \frac{4\pi D_L^2 S_{\rm TeV}}{(1+z)^{2-\Gamma}} \ {\rm erg\,s^{-1}}, \quad (3)$$

where $D_L$ is the luminosity distance in cm, and

$$L_{\rm R} = \frac{4\pi D_L^2 \nu S_\nu}{(1+z)} \ {\rm erg\,s^{-1}}, \quad (4)$$

where $S_\nu$ is the total VLBA flux density in ${\rm erg\,cm^{-2}\,s^{-1}\,GHz^{-1}}$, and $\nu = 8$ GHz. The quantities $F_0$, $E_0$, $\Gamma$, $S_\nu$, and $z$ are tabulated in Table 7. If a photon spectral index was not measured for a source, then we used the median measured photon spectral index of $\Gamma = 3.2$. We assume a flat radio spectral index ($\alpha = 0$) for the radio $k$ correction and luminosity calculation.

The TeV loudness is tabulated in Table 7, and a histogram of this statistic is shown in Figure 5. As can be seen from Figure 5, the distribution spans about two orders of magnitude, from about $10^2$ to $10^4$, but the distribution is peaked around the median value of about $10^3$. A similar range of about two orders of magnitude in gamma-ray loudness is spanned by the BL Lac objects studied by Lister et al. (2011), although much of the range in gamma-ray loudness observed by those authors is due to a mix of HBLs, IBLs, and low-frequency peaked BL Lac objects (LBLs) in the MOJAVE sample. The fact that a similar range is observed here among just the TeV HBLs is mostly due to the inclusion of the radio-faintest TeV HBLs at flux-density levels of a few millijanskys. For example, the single source with TeV loudness greater than $10^4$ in Figure 5 is the extreme blazar H 1426+428, which is among the brighter TeV sources, but it has a VLBA flux density of only about 20 mJy. Conversely, the two sources with TeV loudness less than $10^2$ in Figure 5 are the relatively radio-bright HBLs PKS 0301−243 and 1ES 1741+196.

We might expect there to be a significant anticorrelation between TeV loudness and redshift because of EBL absorption of TeV gamma-rays from distant sources. However, a correlation

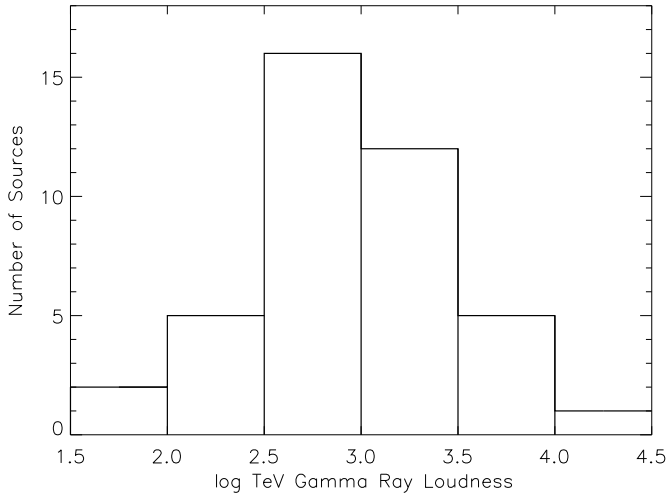


**Figure 5.** Histogram of the TeV loudness for the 41 TeV HBLs from Table 7 with both TeV and VLBI fluxes. The TeV loudness is defined in Section 4.3.

analysis of these two quantities does not yield a significant correlation, possibly because the vast majority of the TeV HBLs are clustered at low redshifts, and these low redshift sources already show a large intrinsic scatter in TeV loudness. Lister et al. (2011) found a significant anticorrelation between gamma-ray loudness and *Fermi* photon spectral index for the BL Lac objects in their sample. We confirm this correlation for the TeV HBLs in this paper at a marginally significant level; for the 35 sources in Table 7 with both measured TeV loudness and photon index, a partial Spearman rank correlation test (excluding effects of redshift) has a significance of 0.03. See Lister et al. (2011) for a discussion of the implications of such a correlation for emission models in BL Lac objects.

### *4.4. Flux–Flux Correlations*

Establishing whether or not blazar fluxes in different wavebands (e.g., radio and gamma-ray) are intrinsically correlated, independent of any common-distance effects, is important to establishing to what degree the emission regions in the jet at these different wavebands are connected. The existence of correlations implies that the emission regions, even if they occur in different components of the jet with different beaming parameters, are related through some physical property of the source. Truly uncorrelated fluxes would instead imply that the emission regions probed by radio and gamma-ray observations are completely independent of each other.

The top panel of Figure 6 shows the TeV flux in milliCrabs versus the total VLBI flux density in millijanskys for the 41 sources in Table 7 with measured TeV and VLBI fluxes. A partial correlation analysis (excluding effects of redshift) gives a Pearson partial correlation coefficient of 0.50 with a significance of $9 \times 10^{-4}$ (99.91% chance of correlation). Repeating the analysis using the VLBI model-fit core flux density instead of the total flux density yields a similar but slightly lower Pearson partial correlation coefficient of 0.48, with a significance of $1.7 \times 10^{-3}$ (99.83% chance of correlation). The correlation with core flux density is probably slightly less significant because the extra step of model fitting introduces some scatter into the core flux density values, particularly when there is a bright jet component close to the core. The high value for the significance of the correlation shown in the top panel of Figure 6 is partly due to the two sources Mrk 421 and Mrk 501, which are bright in both the radio and TeV gamma-rays. However, even if those

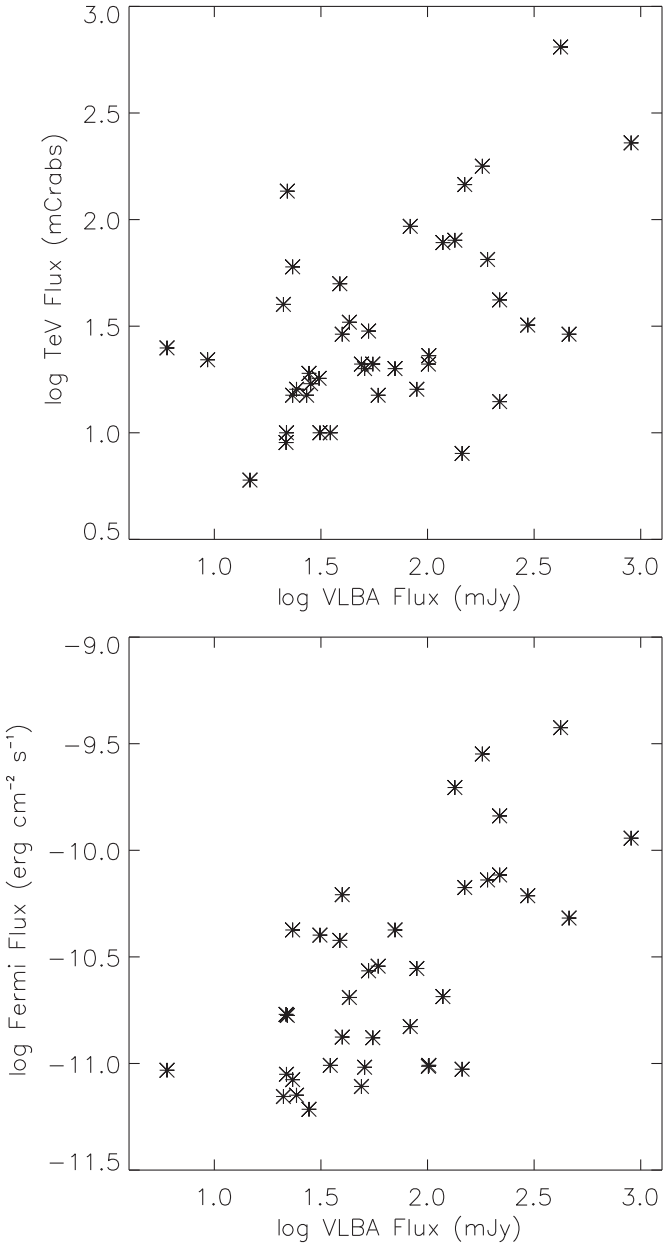


**Figure 6.** Top panel: plot of TeV flux in milliCrabs vs. total VLBA flux density in millijanskys (41 sources). Bottom panel: plot of 2FGL *Fermi* flux vs. total VLBA flux density in millijanskys (37 sources). All flux values are from Table 7.

two sources are excluded (and note that there is no particular physical reason for excluding them), the partial correlation remains significant, although at a lower level of 96.3%. This is the first time, to our knowledge, that a correlation between the TeV flux and the VLBI flux has been established for the TeV HBL population.

To further test the robustness of this new correlation, we employed Monte Carlo simulations using the method described by Pavlidou et al. (2012) to generate intrinsically uncorrelated permutations of the data for comparison purposes, using the monochromatic flux density at 0.3 TeV computed from Table 7 as the TeV flux sample. Because this method requires applying $k$ corrections to the permuted data, the six sources without a TeV photon spectral index in Table 7 were excluded. A comparison of $10^7$ randomly permuted data sets for the 35 remaining sources with the actual data set yields a significance of correlation of

0.056 (94.4% chance of correlation). This result is now only marginally significant; however, Pavlidou et al. (2012) state that their method is conservative for small samples such as this and that existing intrinsic correlations may not be verified. We also note that the noncontemporaneous nature of the data may wash out a stronger correlation that might have existed in concurrently measured data.

The bottom panel of Figure 6 shows the 2FGL *Fermi* flux versus the total VLBI flux density for the 37 sources in Table 7 with measured *Fermi* and VLBI fluxes. A similar plot is shown for the MOJAVE program sources in Figure 1 of Lister et al. (2011), and the bottom panel of Figure 6 basically continues the trend for the HBLs shown in that figure toward lower VLBI and *Fermi* flux values. Correlations between radio and *Fermi* fluxes for larger samples of *Fermi* blazars have been established by a number of authors (e.g., Kovalev et al. 2009; Ackermann et al. 2011; Linford et al. 2012). A correlation between *Fermi* and radio fluxes solely for the TeV HBL subpopulation of *Fermi* sources was claimed by Xiong et al. (2013), although they did not address common-distance effects. We confirm such a correlation between the *Fermi* and VLBI fluxes of the TeV HBLs; a partial correlation analysis (excluding effects of redshift) gives a Pearson partial correlation coefficient of 0.76 with a formal significance of about $10^{-7}$. However, we note that because this sample is TeV-selected rather than *Fermi*-selected, such tests may overestimate the significance of correlations because they do not address upper limits for the TeV HBLs that are not in the 2FGL catalog, although this is a small number of objects (six sources).

### 4.5. Radio Variability and Modulation Indices

The variability of a radio source is an important property (potentially constraining both relativistic beaming and the relative locations of emission regions at different wavebands) that cannot be well studied by sequences of only a few VLBA images. The largest current effort to study radio variability of blazars is the Owens Valley Radio Observatory (OVRO) monitoring program,[9] which presently monitors more than 1800 blazars about twice per week.

The OVRO program's chosen parameter to characterize variability is the intrinsic modulation index, $\overline{m}$, which is an estimate of the standard deviation of the source flux density divided by its mean (Richards et al. 2011, 2014). Although many of the TeV HBLs are in the OVRO program, because of their relative faintness they are clustered near the program's measurement limits in flux density and modulation index. For example, although 25 of the TeV HBLs in Table 7 are in Table 1 of Richards et al. (2014), six do not have a measured modulation index, and another nine have a flux density and modulation index that are excluded from the analysis for being too close to the measurement limits. The 10 remaining high-confidence modulation indices are tabulated with the other source data in Table 7. Because only 10 TeV HBLs pass the current data cuts in the OVRO analysis, we do not attempt correlation studies with the modulation index here, but leave it as an interesting possibility for future study if thresholds for the OVRO variability analysis are lowered.

## 5. DISCUSSION AND CONCLUSIONS

We have investigated the parsec-scale jet structure of 20 relatively newly discovered TeV HBLs that had not been previously well studied with VLBI. These newly discovered TeV HBLs extend down to only a few millijanskys in flux density, so they are not present in large VLBI monitoring programs. All sources were detected and imaged, and all showed parsec-scale jets that could be modeled with at least one Gaussian component (Section 3.2). Most sources had a one-sided core-jet morphology, although we find two cases of apparently two-sided structure (Section 3.1). Many sources show a common morphology of a collimated jet a few milliarcseconds long that transitions to a lower surface brightness, more diffuse jet with a broader opening angle at a few milliarcseconds from the core. These results show that the entire TeV HBL sample, although relatively faint in the radio, is accessible to analysis with current VLBI instruments.

As well as can be determined from only single-epoch images, the analyses presented here support previous conclusions that Lorentz factors in the parsec-scale cores and jets of TeV HBLs are only modestly relativistic. We determined allowed brightness temperature ranges for each core component (Section 3.3) and found that roughly half of the VLBI cores are resolved with brightness temperature upper limits of a few times $10^{10}$ K (Table 5). A Gaussian brightness temperature of $2 \times 10^{10}$ K was consistent with the data for all but one of the sources. Such brightness temperatures do not require any relativistic beaming to reduce them below likely intrinsic limits. The lack of detection of counterjets does place at least a modest limit on the bulk Lorentz factor, although the strongest such constraint we could place was $\gamma \gtrsim 2$. The distribution of apparent opening angles (Section 3.4) is indistinguishable from that of the general gamma-ray blazar population (Pushkarev et al. 2009; Lister et al. 2011), so there is no indication from their jet morphology that these sources are unusually close to the line of sight compared to other gamma-ray blazars. There is thus no evidence from these images that the slow apparent speeds of TeV HBLs are caused by a much closer alignment to the line of sight compared to the apparently faster sources.

The Doppler Crisis for TeV HBLs suggests that their parsec-scale jets are structurally more complex than those of the more powerful blazars and that they require at least two zones of significantly different Lorentz factor to successfully describe them. A consistent picture is emerging of this dichotomy in the jetted AGN population based on multiwavelength studies of large populations, theoretical modeling, and high-resolution imaging with VLBI. In this picture, jets formed in a low-efficiency accretion mode typical of HBLs (Ghisellini et al. 2005, 2009; Meyer et al. 2013b) favor interaction of the jet walls with the external medium, causing the formation of a slow layer. Radiative interaction between the spine and the layer may then decelerate the spine (Ghisellini et al. 2005), producing longitudinal as well as transverse velocity structure, such as postulated by Georganopoulos & Kazanas (2003). Application of such two-zone models can also be successful in reducing the most extreme Doppler factors sometimes required by one-zone models. For example, for the TeV blazar PKS 1424+240, fitting the SED with a one-zone model yields a Doppler factor of ∼100, while the MOJAVE VLBA data imply a Doppler factor of only ∼10 (Aleksić et al. 2014a). When the same SED is fit by the two-zone model of Tavecchio et al. (2011), the Doppler factor of the fast zone is reduced to ∼30, while that of the slower zone has the VLBA-derived value of ∼10 (Aleksić et al. 2014a).

VLBI imaging might detect such two-zone spine-layer jets through observations of transverse emission structures such as limb brightening. We do observe limb brightening in two sources

[9] http://www.astro.caltech.edu/ovroblazars

(see Section 3.5), although for the majority of sources the transverse structure is either unresolved or patchy and complex with multiple emission peaks. However, we note that, because of increased source distance and lower observing frequency, the observations in this paper have about an order of magnitude worse linear resolution than the high-frequency observations of limb brightening in the nearby bright TeV blazars Mrk 421 and Mrk 501 (e.g., Piner et al. 2009, 2010).

In the spine-layer model for TeV HBLs, the TeV emission comes from the spine and the radio emission comes from the layer, causing different Lorentz factors to be measured in the two spectral bands. However, for TeV radio galaxies, both the gamma-ray and the radio emission can be dominated by the layer (Ghisellini et al. 2005), so consistent Lorentz factors might be expected (no Doppler Crisis). VLBI observations of the three known TeV radio galaxies M87 (e.g., Hada et al. 2014), Cen A (e.g., Müller et al. 2014), and 3C 84 (e.g., Nagai et al. 2014) can therefore provide consistency checks on spine-layer models (e.g., Tavecchio & Ghisellini 2008, 2014).

We extended our consideration to the full sample of TeV HBLs in Section 4, by combining our VLBI data on 20 sources from this paper with other VLBI and gamma-ray data from the literature. Following the approach of Lister et al. (2011), we constructed a gamma-ray loudness parameter for the TeV HBLs (Section 4.3) and found that it spans about two orders of magnitude from extreme gamma-ray loud sources like H 1426+428 to more radio-loud sources like PKS 0301−243. There is a significant apparent partial correlation (excluding effects of redshift) between the VLBI and TeV fluxes (Section 4.4), although Monte Carlo simulations using the method of Pavlidou et al. (2012) showed that this correlation may intrinsically be only marginally significant. Such a correlation might suggest that Doppler factors in different jet emission regions are correlated, even if they are significantly different, such as occurs in the model by Lyutikov & Lister (2010). Note that VLBI core flares correlated with gamma-ray flares in Mrk 421 (Richards et al. 2013) also suggest a link between the VLBI emission and the gamma-ray emission in that source.

Much more information about the jet kinematics of the TeV HBLs should be revealed through the multiepoch VLBA monitoring of these 20 sources that is currently underway. At least three additional epochs for each of these sources have been approved on the VLBA and should be obtained over the next one to two years, in addition to high-frequency imaging of some of the brighter TeV HBLs to investigate transverse jet structures. When added to the 11 TeV HBLs that we have already monitored and the seven additional TeV HBLs being monitored by MOJAVE, this will make information on parsec-scale structural changes available for ∼90% of the currently known TeV HBL population. This is a crucial step toward understanding the jet structure of this group of sources, as the high-energy community looks forward to many more such objects being detected by future TeV telescopes like the Cherenkov Telescope Array.

The National Radio Astronomy Observatory is a facility of the National Science Foundation operated under cooperative agreement by Associated Universities, Inc. This research has made use of the NASA/IPAC Extragalactic Database (NED), which is operated by the Jet Propulsion Laboratory, California Institute of Technology, under contract with the National Aeronautics and Space Administration. This research has made use of data from the MOJAVE database that is maintained by the MOJAVE team (Lister et al. 2009). Part of this research was carried out at the Jet Propulsion Laboratory, Caltech, under a contract with the National Aeronautics and Space Administration. This work was supported by Fermi Guest Investigator grant NNX13AO82G. We also acknowledge helpful comments from the anonymous referee.

*Facility:* VLBA

## REFERENCES

Aartsen, M. G., Ackermann, M., Adams, J., et al. 2014, PhRvL, 113, 101101
Abramowski, A., Acero, F., Aharonian, F., et al. 2010a, A&A, 520, A83
Abramowski, A., Acero, F., Aharonian, F., et al. 2010b, A&A, 516, A56
Abramowski, A., Acero, F., Aharonian, F., et al. 2011, A&A, 529, A49
Abramowski, A., Acero, F., Aharonian, F., et al. 2012, A&A, 542, A94
Abramowski, A., Acero, F., Aharonian, F., et al. 2013a, A&A, 554, A72
Abramowski, A., Acero, F., Aharonian, F., et al. 2013b, A&A, 559, A136
Abramowski, A., Acero, F., Aharonian, F., et al. 2013c, MNRAS, 434, 1889
Abramowski, A., Acero, F., Akhperjanian, A. G., et al. 2013d, A&A, 552, A118
Acciari, V., Aliu, E., Arlen, T., et al. 2009a, ApJL, 690, L126
Acciari, V. A., Aliu, E., Arlen, T., et al. 2009b, ApJ, 695, 1370
Acciari, V. A., Aliu, E., Arlen, T., et al. 2010, ApJL, 715, L49
Acciari, V. A., Aliu, E., Arlen, T., et al. 2011a, ApJ, 738, 169
Acciari, V. A., Arlen, T., Aune, T., et al. 2011b, ApJ, 729, 2
Acero, F., Aharonian, F., Akhperjanian, A. G., et al. 2010, A&A, 511, A52
Ackermann, M., Ajello, M., Allafort, A., et al. 2011, ApJ, 741, 30
Aharonian, F., Akhperjanian, A. G., Anton, G., et al. 2010, A&A, 521, A69
Aharonian, F., Akhperjanian, A. G., Barres de Almeida, U., et al. 2007a, A&A, 473, L25
Aharonian, F., Akhperjanian, A. G., Barres de Almeida, U., et al. 2008, A&A, 481, L103
Aharonian, F., Akhperjanian, A. G., Bazer-Bachi, A. R., et al. 2006, A&A, 457, 899
Aharonian, F., Akhperjanian, A. G., Bazer-Bachi, A. R., et al. 2007b, A&A, 470, 475
Aharonian, F., Akhperjanian, A. G., Bazer-Bachi, A. R., et al. 2007c, ApJL, 664, L71
Albert, J., Aliu, E., Anderhub, H., et al. 2006a, ApJL, 648, L105
Albert, J., Aliu, E., Anderhub, H., et al. 2006b, ApJ, 639, 761
Albert, J., Aliu, E., Anderhub, H., et al. 2007a, ApJL, 667, L21
Albert, J., Aliu, E., Anderhub, H., et al. 2007b, ApJ, 663, 125
Albert, J., Aliu, E., Anderhub, H., et al. 2007c, ApJ, 669, 862
Aleksić, J., Alvarez, E. A., Antonelli, L. A., et al. 2012a, A&A, 544, A142
Aleksić, J., Alvarez, E. A., Antonelli, L. A., et al. 2012b, ApJ, 748, 46
Aleksić, J., Alvarez, E. A., Antonelli, L. A., et al. 2012c, A&A, 539, A118
Aleksić, J., Ansoldi, S., Antonelli, L. A., et al. 2014a, A&A, 567, A135
Aleksić, J., Antonelli, L. A., Antoranz, P., et al. 2010, ApJL, 723, L207
Aleksić, J., Antonelli, L. A., Antoranz, P., et al. 2013, A&A, 556, A67
Aleksić, J., Antonelli, L. A., Antoranz, P., et al. 2014b, A&A, 563, A90
Aliu, E., Archambault, S., Arlen, T., et al. 2012a, ApJ, 750, 94
Aliu, E., Archambault, S., Arlen, T., et al. 2012b, ApJ, 755, 118
Aliu, E., Archambault, S., Arlen, T., et al. 2014, ApJ, 782, 13
Aliu, E., Aune, T., Beilicke, M., et al. 2011, ApJ, 742, 127
Archambault, S., Aune, T., Behera, B., et al. 2014, ApJL, 785, L16
Barkov, M. V., Aharonian, F. A., Bogovalov, S. V., Kelner, S. R., & Khangulyan, D. 2012, ApJ, 749, 119
Becherini, Y., Boisson, C., Cerruti, M., et al. 2012, in AIP Proc. 1505, High Energy Gamma-Ray Astronomy: 5th International Meeting on High Energy Gamma-Ray Astronomy, ed. F. A. Aharonian, W. Hofmann, & F. M. Rieger (Melville, NY: AIP), 490
Begelman, M. C., Fabian, A. C., & Rees, M. J. 2008, MNRAS, 384, L19
Benbow, W. 2011, in 32nd ICRC, 8, 51
Berger, K. 2011, in 32nd ICRC, 8, 169
Blasi, M. G., Lico, R., Giroletti, M., et al. 2013, A&A, 559, A75
Bourda, G., Charlot, P., Porcas, R. W., & Garrington, S. T. 2010, A&A, 520, A113
Britzen, S., Vermeulen, R. C., Campbell, R. M., et al. 2008, A&A, 484, 119
Chiaberge, M., Celotti, A., Capetti, A., & Ghisellini, G. 2000, A&A, 358, 104
Clausen-Brown, E., Lyutikov, M., & Kharb, P. 2011, MNRAS, 415, 2081
Cortina, J. 2013a, ATel, 5038, 1
Cortina, J. 2013b, ATel, 5080, 1
Croke, S. M., O'Sullivan, S. P., & Gabuzda, D. C. 2010, MNRAS, 402, 259
De Lotto, B. 2012, JPhCS, 375, 052021
Edwards, P. G., & Piner, B. G. 2002, ApJL, 579, L67
Gabányi, K. É., Dubner, G., Giacani, E., et al. 2013, ApJ, 762, 63

Georganopoulos, M., & Kazanas, D. 2003, ApJL, 594, L27
Ghisellini, G., Maraschi, L., & Tavecchio, F. 2009, MNRAS, 396, L105
Ghisellini, G., Tavecchio, F., & Chiaberge, M. 2005, A&A, 432, 401
Giannios, D., Uzdensky, D. A., & Begelman, M. C. 2009, MNRAS, 395, L29
Giroletti, M., Giovannini, G., Cotton, W. D., et al. 2008, A&A, 488, 905
Giroletti, M., Giovannini, G., Feretti, L., et al. 2004a, ApJ, 600, 127
Giroletti, M., Giovannini, G., Taylor, G. B., & Falomo, R. 2004b, ApJ, 613, 752
Giroletti, M., Giovannini, G., Taylor, G. B., & Falomo, R. 2006, ApJ, 646, 801
Hada, K., Giroletti, M., Kino, M., et al. 2014, ApJ, 788, 165
Henri, G., & Pelletier, G. 1991, ApJL, 383, L7
Holder, J. 2012, APh, 39, 61
Holder, J. 2014, BrJPh, 44, 450
Homan, D. C., Kovalev, Y. Y., Lister, M. L., et al. 2006, ApJL, 642, L115
Horan, D., Badran, H. M., Bond, I. H., et al. 2002, ApJ, 571, 753
Hovatta, T., Leitch, E. M., Homan, D. C., et al. 2013, Eur. Phys. J. Web Conf., 61, 6005
Kellermann, K. I., & Pauliny-Toth, I. I. K. 1969, ApJL, 155, L71
Kovalev, Y. Y., Aller, H. D., Aller, M. F., et al. 2009, ApJL, 696, L17
Kovalev, Y. Y., Kellermann, K. I., Lister, M. L., et al. 2005, AJ, 130, 2473
Lähteenmäki, A., Valtaoja, E., & Wiik, K. 1999, ApJ, 511, 112
Lico, R., Giroletti, M., Orienti, M., et al. 2012, A&A, 545, A117
Linford, J. D., Taylor, G. B., Romani, R. W., et al. 2012, ApJ, 744, 177
Lister, M. L., Aller, M., Aller, H., et al. 2011, ApJ, 742, 27
Lister, M. L., Cohen, M. H., Homan, D. C., et al. 2009, AJ, 138, 1874
Lobanov, A. P. 2005, A&A, submitted (arXiv:astro-ph/0503225)
Lovell, J. 2000, in Astrophysical Phenomena Revealed by Space VLBI, ed. H. Hirabayashi, P. G. Edwards, & D. W. Murphy (Sagamihara: ISAS), 301
Lovell, J. E. J., Horiuchi, S., Moellenbrock, G., et al. 2000, in Astrophysical Phenomena Revealed by Space VLBI, ed. H. Hirabayashi, P. G. Edwards, & D. W. Murphy (Sagamihara: ISAS), 183
Lyutikov, M., & Lister, M. 2010, ApJ, 722, 197
Mariotti, M. 2011, ATel, 3719, 1
Marscher, A. P. 2013, EPJWC, 61, 04001
Martí-Vidal, I., & Marcaide, J. M. 2008, A&A, 480, 289
Mazin, D. 2012, in AIP Conf. Ser. 1505, High Energy Gamma-Ray Astronomy: 5th International Meeting on High Energy Gamma-Ray Astronomy, ed. F. A. Aharonian, W. Hofmann, & F. M. Rieger (Melville, NY: AIP), 186
Meyer, E. T., Fossati, G., Georganopoulos, M., & Lister, M. L. 2011, ApJ, 740, 98
Meyer, E. T., Georganopoulos, M., Fossati, G., & Lister, M. L. 2013a, EPJWC, 61, 05002
Meyer, E. T., Georganopoulos, M., Fossati, G., & Lister, M. L. 2013b, BAAS, 13, 111.03
Mirzoyan, R. 2014a, ATel, 5768, 1
Mirzoyan, R. 2014b, ATel, 6062, 1
Müller, C., Kadler, M., Ojha, R., et al. 2014, A&A, 569, A115
Nagai, H., Haga, T., Giovannini, G., et al. 2014, ApJ, 785, 53
Nalewajko, K., Giannios, D., Begelman, M. C., Uzdensky, D. A., & Sikora, M. 2011, MNRAS, 413, 333
Narayan, R., & Piran, T. 2012, MNRAS, 420, 604
Nolan, P. L., Abdo, A. A., Ackermann, M., et al. 2012, ApJS, 199, 31
Pavlidou, V., Richards, J. L., Max-Moerbeck, W., et al. 2012, ApJ, 751, 149
Pearson, T. J. 1995, in ASP Conf. Ser. 82, Very Long Baseline Interferometry and the VLBA, ed. J. A. Zensus, P. J. Diamond, & P. J. Napier (San Francisco, CA: ASP), 268
Piner, B. G., & Edwards, P. G. 2004, ApJ, 600, 115
Piner, B. G., & Edwards, P. G. 2013, EPJWC, 61, 04021
Piner, B. G., Edwards, P. G., Wehrle, A. E., et al. 2000, ApJ, 537, 91
Piner, B. G., Mahmud, M., Fey, A. L., & Gospodinova, K. 2007, AJ, 133, 2357
Piner, B. G., Pant, N., & Edwards, P. G. 2008, ApJ, 678, 64
Piner, B. G., Pant, N., & Edwards, P. G. 2010, ApJ, 723, 1150
Piner, B. G., Pant, N., Edwards, P. G., & Wiik, K. 2009, ApJL, 690, L31
Piner, B. G., Pushkarev, A. B., Kovalev, Y. Y., et al. 2012, ApJ, 758, 84
Piner, B. G., Unwin, S. C., Wehrle, A. E., et al. 1999, ApJ, 525, 176
Prandini, E., Bonnoli, G., & Tavecchio, F. 2012, A&A, 543, A111
Pushkarev, A. B., Kovalev, Y. Y., Lister, M. L., & Savolainen, T. 2009, A&A, 507, L33
Readhead, A. C. S. 1994, ApJ, 426, 51
Rector, T. A., Gabuzda, D. C., & Stocke, J. T. 2003, AJ, 125, 1060
Richards, J. L., Hovatta, T., Lister, M. L., et al. 2013, EPJWC, 61, 04010
Richards, J. L., Hovatta, T., Max-Moerbeck, W., et al. 2014, MNRAS, 438, 3058
Richards, J. L., Max-Moerbeck, W., Pavlidou, V., et al. 2011, ApJS, 194, 29
Romney, J. D., Brisken, W. F., Durand, S. J., & Walker, R. C. 2009, in 2009 USNC/URSI Annual Meeting
Sahayanathan, S. 2009, MNRAS, 398, L49
Sakamoto, Y., Nishijima, K., Mizukami, T., et al. 2008, ApJ, 676, 113
Tavecchio, F., Becerra-Gonzalez, J., Ghisellini, G., et al. 2011, A&A, 534, A86
Tavecchio, F., & Ghisellini, G. 2008, MNRAS, 385, L98
Tavecchio, F., & Ghisellini, G. 2014, MNRAS, 443, 1224
Tavecchio, F., Ghisellini, G., Ghirlanda, G., Foschini, L., & Maraschi, L. 2010, MNRAS, 401, 1570
Tavecchio, F., Ghisellini, G., & Guetta, D. 2014, ApJL, 793, L18
Tiet, V. C., Piner, B. G., & Edwards, P. G. 2012, in 2012 Fermi & Jansky Proceedings—eConf C1111101, arXiv:1205.2399
Tingay, S. J., Preston, R. A., Lister, M. L., et al. 2001, ApJL, 549, L55
Wehrle, A. E., Piner, B. G., Unwin, S. C., et al. 2001, ApJS, 133, 297
Xiong, D., Zhang, H., Zhang, X., et al. 2013, Ap&SS, 343, 345